

Random quantum circuits with time-reversal symmetry

Kabir Khanna^{1,2}, Abhishek Kumar², Romain Vasseur^{1,*} and Andreas W. W. Ludwig³

¹*Department of Theoretical Physics, University of Geneva, 24 quai Ernest-Ansermet, 1211 Genève, Switzerland*

²*Department of Physics, University of Massachusetts, Amherst, Massachusetts 01003, USA*

³*Department of Physics, University of California, Santa Barbara, California 93106, USA*



(Received 11 April 2025; accepted 27 November 2025; published 12 February 2026)

Time-reversal (TR) symmetry is crucial for understanding a wide range of physical phenomena, and plays a key role in constraining fundamental particle interactions and in classifying phases of quantum matter. In this work, we introduce an ensemble of random quantum circuits that are representative of the dynamics of generic TR-invariant many-body quantum systems. We derive a general statistical mechanics model describing entanglement, many-body quantum chaos, and quantum information dynamics in such TR-invariant circuits. As an example of application of our formalism, we study the universal properties of measurement-induced phase transitions in monitored TR-invariant systems, with measurements performed in a TR-invariant basis. We find that TR invariance of the unitary part of the dynamics does not affect the universality class, unless measurement outcomes are postselected to satisfy the global TR invariance of each quantum trajectory. We confirm these predictions numerically and find, for both generic and Clifford-based evolutions, critical exponents in the case of “strong,” i.e., global TR invariance where each quantum trajectory is TR invariant.

DOI: [10.1103/4bgj-p2jk](https://doi.org/10.1103/4bgj-p2jk)

I. INTRODUCTION

Generic isolated many-body systems undergoing unitary dynamics thermalize by scrambling locally encoded information into nonlocal degrees of freedom [1–4]. In contrast, open quantum systems can be modeled by two competing processes: unitary evolution, which scrambles information, and nonunitary generalized measurements due to noisy coupling with the environment, which attempt to extract quantum information from the system. Understanding the universal features of this competition presents a key challenge. Recent experimental progress with digital and noisy-intermediate scale quantum simulators has further accelerated theoretical advancements in this area [5,6]. Minimally structured models that can naturally be implemented on these platforms and capture the relevant physics include quantum circuits with random local unitary gates and measurements. The randomness in these circuits often allows for theoretical tractability by mapping specific problems to effective classical descriptions. Consequently, these systems have been instrumental in uncovering many universal phenomena associated with the dynamics of quantum information, even in the absence of symmetries. This includes Kardar-Parisi-Zhang universality [7] of entanglement growth [8,9], its connection to the Ryu-Takayanagi formula in holography [10,11], and the hy-

drodynamical nature of operator spreading [12,13] among others.

By adding local quantum measurements to the dynamics, an intriguing dynamical phase transition appears in the quantum trajectories as the measurement rate increases, known as a measurement-induced phase transition (MIPT) [14,15]. Crucially, this transition is only visible in properties of a quantum state *conditional* on a set of measurement outcomes—it is invisible if measurement outcomes are discarded (or traced over). The MIPT phases are distinguished by the entanglement properties of quantum trajectories: At low measurement rates, entanglement follows a volume law, while at high rates, it obeys an area law. Interestingly, this transition can be understood from multiple perspectives. One such perspective is the purification transition, where a mixed state remains mixed in the volume law phase but is purified in the area law phase [16]. Another viewpoint comes from the lens of quantum error correction: The volume law phase serves as an efficient error-correcting code, encoding information nonlocally and safeguarding it from local errors (measurements) [17]. Lastly, this transition can also be understood from the perspective of the observer, in terms of “learnability” of the initial state [16–19]. In the area law phase, measurement outcomes contain enough information to help distinguish between two states, whereas in the volume law phase, the outcomes are essentially random, making it impossible to infer the difference between them.

MIPTs have been studied extensively in a variety of contexts both numerically and theoretically in the past few years, establishing them as a generic property of monitored quantum systems [16–92] (also see Refs. [93,94] for reviews on the subject). The credibility of these studies is further supported by experimental observations of MIPTs in numerous experimental setups [95–99]. A particularly important theoretical

*Contact author: romain.vasseur@unige.ch

Published by the American Physical Society under the terms of the [Creative Commons Attribution 4.0 International license](https://creativecommons.org/licenses/by/4.0/). Further distribution of this work must maintain attribution to the author(s) and the published article’s title, journal citation, and DOI.

tool developed to understand and characterize these transitions has been to map them into effective stat-mech models using the replica trick, a procedure that was first outlined in the study of random tensor networks [100,101] and was subsequently adopted for unitary and hybrid circuits [9,102–104]. These mappings are *exact*, allowing us to study information theoretic features of the ensemble averaged dynamics from the lens of equilibrium statistical mechanics. The need for the replica trick here emerges when dealing with observables that are inherently nonlinear in the density matrix. An example of the utility of these stat-mech mappings is the understanding of the entanglement transition as a symmetry breaking transition. Here, the volume law corresponds to the symmetry-broken phase, while the area law reflects a disordered phase. Entanglement scaling, say in the volume law phase, is then understood as resulting from the domain wall line tension at the boundary.

An important area of research within random quantum circuits has focused on using these tools to explore the effects of introducing global symmetry into the system. Previous studies on Abelian symmetries such as $U(1)$ and non-Abelian symmetries such as $SU(2)$ have revealed interesting physics [105–109]. Notably, there can exist a “charge sharpening” transition, where each phase differs based on how effectively an observer can learn about global quantum numbers from local measurements [47,108,110,111].

In contrast to these internal symmetries, the role of fundamental symmetries such as time-reversal (TR) on the dynamics of quantum information remains relatively unexplored. Historically, this approach underpinned Dyson’s threefold classification of random matrix ensembles, of which TR (“orthogonal” ensemble) was a central class [112]. More recently, Zirnbauer [113] and Altland and Zirnbauer [114] enumerated all possible symmetry classes of random matrices and of Hamiltonians of noninteracting fermionic systems. There were ten classes in total, including the three classes Dyson introduced. TR symmetry was again used here as one of a complete set of antiunitary symmetries that enable an exhaustive classification of all Hamiltonians modulo unitarily implemented symmetries [115] (for a basic review, see, e.g., Ref. [116]). This exhaustive list of symmetry classes then culminated in the “tenfold way” classification of topological insulators and superconductors for noninteracting fermions [117,118]. Finally, TR symmetry also played a crucial role in the classification of topological phases in interacting systems (see, e.g., Refs. [119,120]). For an approach, which is different from the logic presented in the present paper, using the “tenfold way” for the classification of nonunitary circuit evolutions of noninteracting fermions, see Ref. [40]. For related work in a somewhat different context, see Ref. [121]. Given such historical significance of TR, in this paper we explore the dynamics of TR-invariant chaotic quantum systems where the (antiunitary) time-reversal operator \mathcal{T} squares to plus the identity, $\mathcal{T}^2 = +1$ (“orthogonal class”), using the toolbox of random quantum circuits. (In this paper, we only consider for simplicity this particular time-reversal symmetry, referring to it simply as TR symmetry from now on. Circuits invariant under the time-reversal operation where $\mathcal{T}^2 = -1$ will be treated in future work.) As we review in Sec. II, imposing TR invariance leads to selecting

gates from the circular orthogonal ensemble (COE), which consists of all symmetric unitary matrices and is thus invariant under $U \rightarrow U^T U U$, where U is a fixed unitary. We make a crucial distinction between “local TR invariance” and “global TR invariance,” notions we detail in Sec. II. Essentially, local TR invariance refers to models where each gate used in the evolution is sampled from the COE, and is naturally generated by a TR-invariant Hamiltonian. There is a natural reason to study such local TR setups, namely, that any evolution generated by the Trotterized version of a TR-invariant Hamiltonian would have local TR invariance. Global TR invariance on the other hand puts restriction on the whole evolution of the entire circuit being TR symmetric.

The key result of our work is a general mapping of the calculation of the dynamics of Rényi entropies in TR-invariant quantum circuits onto a replica statistical mechanics model. This mapping generalizes the approach of Refs. [9,102,103], but involves averaging over moments of COE matrices instead of over unitary matrices, performed graphically using results from the corresponding random matrix theory detailed in Ref. [122]. The resulting statistical mechanics model features nonlocal Boltzmann weights, differing qualitatively from the familiar statistical mechanics model of the canonical unitary Haar ensemble. This mapping provides the first step toward studying properties of many-body chaos under TR-invariant unitary evolution using the tools of random quantum circuits, including, e.g., operator spreading and entanglement dynamics.

As an example of application of this framework, we then study MIPTs in monitored TR-invariant quantum dynamics. Here, the measurements are performed in a TR-invariant basis, where the measurement outcomes “on average” preserve the TR invariance of the dynamics. One might then expect a universality class to emerge. However, we find that the universality class of the MIPT remains the same as in the generic, non-TR-symmetric model, as random measurement outcomes break TR invariance in individual trajectories. On the other hand, if we postselect measurement outcomes so each quantum trajectory is individually TR invariant (“strong” global symmetry), we predict that a universality class emerges. We interpret these results in terms of the symmetry of the underlying statistical mechanics models. We note that in a “folded” formulation of the circuit with “strong” global TR symmetry, the postselection requirement of measurement outcomes is replaced by working with the second tensor power of the evolution operator of the first half of the circuit in a doubled Hilbert space and no postselection (Sec. IV B 2). Our findings are supported by numerical results from both Haar and Clifford versions of these circuits, identifying the critical points and distinguishing the aforementioned universality classes. Finally, we note that there have been previous works that have studied random quantum circuits with TR by sampling the gates from COE [123,124]. However, those works do not discuss any critical features of the measurement-induced transition. More importantly, they fail to address the key distinction between global and local time-reversal symmetry, a topic that forms a significant part of our discussion. Finally, we note that the notion of TR discussed in our work arises essentially from requiring a solution to the Schrödinger equation

invariant under the transformation $t \rightarrow -t$. This should not be confused with the fundamentally different setup of a literal reversal of dynamics generated by a unitary U through the subsequent application of the unitary U^\dagger , as discussed, e.g., in Refs. [125–127].

The plan for the remainder of this work is as follows: In Sec. II, we discuss TR symmetry, distinguishing between local and global TR. Section III presents the stat-mech mappings for both the local and global TR models, for purely unitary evolution, i.e., in the absence of measurements. Section IV applies these models to analyze MITs, discussing symmetry properties, universality, and the analytically tractable limit of large onsite Hilbert space dimension d . Finally, Sec. V presents numerical results for both Haar and Clifford circuits. We end with Sec. VI where we summarize our findings and discuss their broader implications.

II. TIME-REVERSAL INVARIANT QUANTUM DYNAMICS

We consider a one-dimensional many-body quantum system of qudits with Hilbert space $\mathcal{H} = (\mathbb{C}^d)^{\otimes L}$. We are broadly interested in the dynamics of quantum information in the case where this system is invariant under time reversal. More generally, we will also consider monitored TR-invariant systems—where the randomness of the measurement outcomes breaks TR invariance in each quantum trajectory, but where the unitary part of the dynamics is TR invariant.

For concreteness, let us begin by focusing on continuous time dynamics generated by a Hamiltonian H . Without measurements, the unitary time evolution $|\psi(t)\rangle = e^{-iHt}|\psi_0\rangle$ is TR invariant if and only if the time-reversal operator \mathcal{T} applied to the backward time-evolved state $|\psi(-t)\rangle = e^{+iHt}|\psi_0\rangle$ is equal to the state resulting from forward evolving the state $\mathcal{T}|\psi_0\rangle$ by a time t , $\mathcal{T}e^{+iHt}|\psi_0\rangle = e^{-iHt}\mathcal{T}|\psi_0\rangle$ (e.g., Ref. [128]). Since this is true for all kets $|\psi_0\rangle$, we obtain $\mathcal{T}H\mathcal{T}^{-1} = H$. To process this condition further, we recall that for any fixed orthonormal basis of Hilbert space, the antiunitary operator \mathcal{T} can be written in the form $\mathcal{T} = \hat{U}_0\hat{K}$, where \hat{K} is the complex conjugation operation (which complex-conjugates the expansion coefficients of each ket in the given basis) and \hat{U}_0 is a fixed, but basis-dependent unitary operator. Note that while both \hat{U}_0 and \hat{K} are basis dependent, $\mathcal{T} = \hat{U}_0\hat{K}$ is not. In particular, in our case of interest where $\mathcal{T}^2 = +1$, there exists [129] a TR-invariant orthonormal basis $\{|i\rangle\}_i$ where $\hat{U}_0 = 1$, and thus $\mathcal{T}|i\rangle = |i\rangle$. In this basis, the TR-invariance condition thus simplifies to $\mathcal{T}H\mathcal{T}^{-1} = \hat{K}H\hat{K}^{-1} = H$, implying that the matrix $H_{ij} = \langle i|H|j\rangle$ is real and symmetric. In turn, this implies that the unitary evolution operator $U(t) = e^{-iHt}$ in this basis is a unitary (in general complex) and symmetric matrix $U_{ij} = \langle i|U(t)|j\rangle$. One can prove [129] that any unitary (in general complex) symmetric matrix is of the form $V^T V$ with V being some unitary matrix. This representation shows that the set of unitary symmetric matrices coincides with the Cartan class AI coset space $U(N)/O(N)$ with N the dimension of the Hilbert space, as $V^T V$ is manifestly invariant under $V \rightarrow OV$ for any orthogonal matrix $O \in O(N)$ [113,114,117,118,130,131]. The set of such matrices is called the COE.

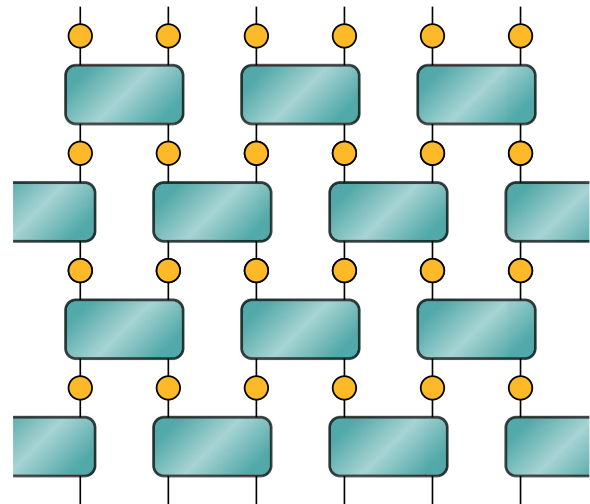


FIG. 1. Monitored TR-invariant system. Physical setup considered in this paper of a weakly monitored TR-invariant one-dimensional quantum system. Upon Trotterization, we obtain a quantum circuit with symmetric gates $U^T = U$, which are all identical as indicated by their color.

Next, we Trotterize the time evolution generated by a (generic, i.e., “nonintegrable”) Hamiltonian H , discussed in the preceding paragraph, as sketched in Fig. 1. It is straightforward to show that each gate is unitary symmetric, and thus belongs to the COE. (The gates are all the same.) Upon adding weak measurements interspersed between these symmetric gates, this setup defines the dynamics of a continuously monitored TR-invariant system. These measurements are performed in the TR-invariant basis, and are thus on average TR invariant. Nevertheless, note that such measurements still break the global TR invariance of the evolution, unless the measurement outcomes obey a mirror symmetry in time—we will come back to this later. Even so, the TR invariance of the underlying unitary evolution still manifests itself by having the gates be represented by unitary symmetric matrices in the TR-invariant basis.

To make analytic progress, we then move away from this Hamiltonian setting, and make the gates random in space and and time, drawn from the COE. This additional randomness can be motivated by considering that the measurement outcomes are random anyway, so further making the gates random does not break any additional symmetries. However, it is important to note that even though each local gate is independently symmetric and thus TR invariant, the global evolution operator of the resulting quantum circuit is *not* TR invariant even in the absence of measurements. We will denote this setup as “locally TR invariant,” referring to the fact that each local gate by itself implements a TR-invariant time evolution. In order for the global time evolution to be TR invariant (“global TR invariance”) even in the absence of measurements, we further need the gates to obey a mirror symmetry in time, as illustrated in Fig. 2. In that case, the total time evolution operator (in the TR-invariant basis) is of the form $U = U_1 U_2 \cdots U_k U_k \cdots U_2 U_1$, where all U_i are (complex) unitary symmetric matrices, which can be rewritten as $U = V^T V$ with $V = U_k \cdots U_2 U_1$. In the rest of this paper,

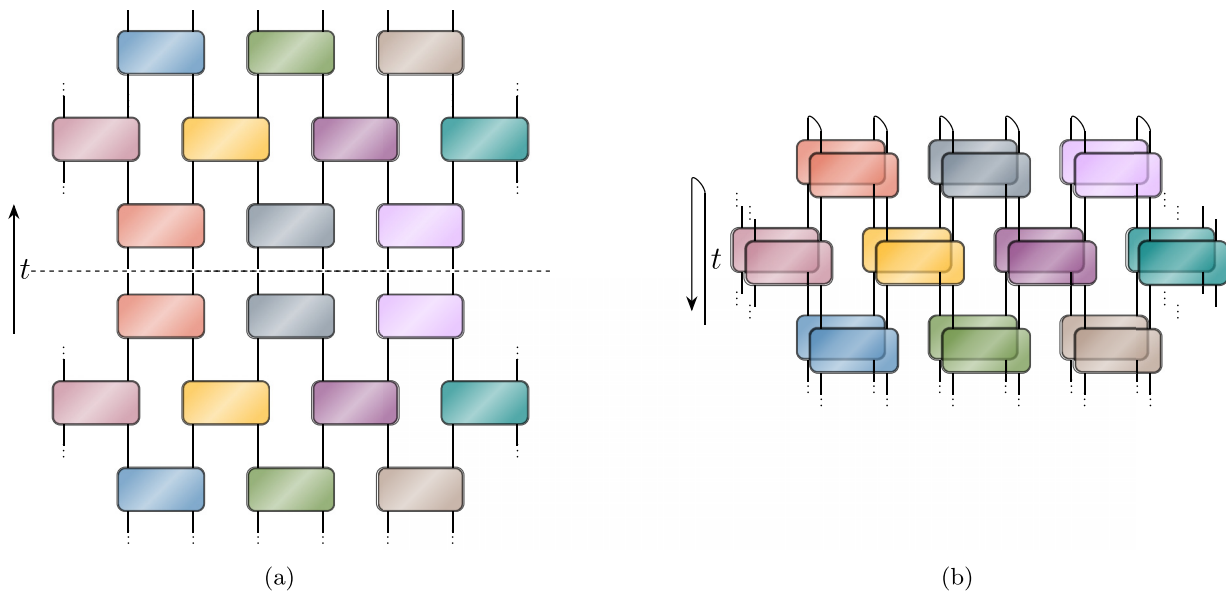


FIG. 2. Circuit representing Global and Local TR evolution: The color of the gates indicates whether they are identical or not. Local TR dynamics is implemented by picking the gates to be of the form $U = V^T V$. The global TR dynamics is implemented by making the full circuit have the structure $V^T V$, as indicated by the mirrored color of the gates. (a) Circuit laid out in a sheet geometry as indicated by the flow of time. (b) The same circuit visualized in a folded geometry as shown by the flow of time. This provides a clear approach to average over nonlocally spaced gates.

we will derive statistical mechanics mappings capturing the dynamics of quantum information in quantum circuits that are either locally, or both globally and locally TR invariant. Note that we will not consider the case of “global but not local” TR invariance, where the total time evolution operator $U = V^T V$ is symmetric, but local gates are not. Throughout this paper, we have in mind a setting where local gates are generated by a TR-invariant Hamiltonian as in Fig. 1, and are thus symmetric. We however comment on the universality of the “global but not local” model in Sec. IV C 2.

We close this section by emphasizing again that, in the absence of measurements, the globally TR-invariant random unitary circuit introduced above represents a random circuit formulation of generic TR-invariant unitary dynamics, in the same sense in which the Haar random unitary circuit [8,12,13] represents a random circuit formulation of generic unitary dynamics breaking time-reversal symmetry. In the case with time-reversal invariance, the *global* TR-invariance condition is essential for this to be the case.

III. STATISTICAL MECHANICS MAPPINGS (NO MEASUREMENTS)

In this section, we derive a replica statistical mechanics model for the dynamics of quantum information under local or global unitary TR-invariant evolution. (We discuss measurements in the subsequent Sec. IV.) We first discuss averaging over moments of COE gates and employ this to derive the stat-mech model for the local TR case. We then impose an additional global TR symmetry, corresponding to a mirror symmetry in time, and derive the corresponding stat-mech model in that case as well.

A. Setup

We consider a 1D chain of length L , qudit of dimension d with the initial state $\rho_0 = |\psi_0\rangle\langle\psi_0|$, where we hereon always work in the TR-invariant basis defined in Sec. II. We subject it to discrete-time dynamics generated by a brickwork random quantum circuit with gates drawn from the COE. We express the gates in the manifestly symmetric basis $U = V^T V$, where $V \in U(D)$ with $D := d^2$ is sampled from the Haar ensemble.

Using the vectorized notation $\rho \rightarrow |\rho\rangle\rangle$, the evolution of the density matrix $|\rho\rangle\rangle_{t-1}$ at time $(t-1)$ to $|\rho\rangle\rangle_t$ at time t can then be written as $|\rho\rangle\rangle_t = U_t \otimes U_t^* |\rho\rangle\rangle_{t-1} = (V_t^T V_t) \otimes (V_t^T V_t)^* |\rho\rangle\rangle_{t-1}$, where $U_t = V_t^T V_t$ is the unitary matrix applied at time step t expressed in the TR-invariant basis. Note that in addition to the doubling of U_t due to ket (U_t) and bra (U_t^*) components of the density matrix evolution, we also here have an additional doubling due to U_t itself being expressed as $V_t^T V_t$.

One can study various quantities to probe universal features of such dynamics. A nonlinear quantity such as the n^{th} Rényi entanglement $S_{n,A}$ entropy of $\rho_A = \text{tr}_{\bar{A}}(\rho)$ is a useful one to demonstrate the stat-mech mapping. It is written as

$$S_{n,A} = \frac{1}{1-n} \ln(\text{tr} \rho_A^n). \quad (1)$$

More precisely, we are interested in the ensemble average denoted by $\bar{S}_{n,A}$ that can be computed using the replica trick [9,101–103]:

$$\bar{S}_{n,A} = \lim_{k \rightarrow 0} \frac{1}{(1-n)} \frac{d}{dk} \mathbb{E}_U [\text{tr}(\rho_A^n)^{\otimes k}], \quad (2)$$

where \mathbb{E}_U is the average over all possible evolutions generated by the COE gates U that are implicit in ρ . Here, we define the

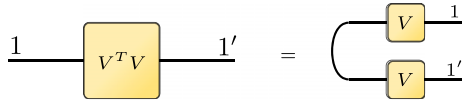


FIG. 3. Input and output legs of a given gate labeled by primed and unprimed numbers, respectively.

quantity

$$Z_A := \mathbb{E}_U [\text{Tr}(\rho^{\otimes nk} S_{A,n}^{\otimes k})], \quad (3)$$

where $S_{A,n}$ is the swap operator that implements the partial trace within region A and the matrix multiplication of the n -fold replicated density matrices within region A in each of the k replicas. For clarity, we hereon use the notation $N = nk$ to denote the total number of copies of the density matrix ρ to be averaged over. Next, one can formally represent the above swap operation on this n -fold replicated space as

$$\mathcal{S}_{A,n} = \prod_x \sum_{\{i\}} |i_{g_x(1)} i_{g_x(2)} \dots i_{g_x(n)}\rangle \langle i_1 i_2 \dots i_n|, \quad (4)$$

$$g_x = \begin{cases} (123 \dots n), & x \in A, \\ e & x \in \bar{A}. \end{cases} \quad (5)$$

Here, $|i\rangle$ represents the TR-invariant basis states in the Hilbert space $\mathcal{H} := (\mathbb{C}^d)^{\otimes L}$, and we have utilized cycle notation for permutations. (e denotes the identity permutation.) Note that we have used the notation Z_A in Eq. (3) anticipating it to correspond to the partition function of the statistical mechanics model that we shall now describe.

B. COE averaging and Boltzmann weights—local TR symmetry

The main expression needed to compute the partition function Z_A is $\mathbb{E}_{U \in \text{COE}}(U^{\otimes N} \otimes U^{*\otimes N})$. This problem of averaging over moments of gates sampled from the COE has been previously solved in Ref. [122]. In this work, we recast the averaging into a more intuitive graphical form, while still utilizing analytic results therein.

A natural approach to this problem is to reduce the problem of averaging over COE gates to the standard Haar average of the unitary group. To achieve this, we treat the gate $V^T V$ as two copies of the unitary gate V with a pair of legs contracted. Graphically with primed numbers for the input legs and unprimed numbers for the output legs. (See Fig. 3) Since there are two sources of doubling—one from the bra/ket and another from expressing gates as a product of V and V^T —we use different colors for the gates in the bra and ket to make the computations clear. We also sometimes color the links with the color of the gate they originate from wherever necessary [see, for example, Eq. (7)]. The above trick makes it clear that we can treat the problem of averaging over $U^{\otimes N} \otimes U^{*\otimes N}$ as averaging over twice the number of copies of the Haar random gate V , with the condition that the legs of the two copies of V stemming from the same symmetric unitary U be contracted (in both, the ket and the bra), as shown in the figure above and also in Eq. (6). The averaging is best illustrated graphically as

follows (here $N = 2$):

Above, the well-known expression for (unitary) Haar averages was used which brings in the Weingarten function $\text{Wg}_D(\tau\sigma^{-1})$ for the unitary group $U(D)$,

$$\int_{\text{Haar}} d\mu(V) V_{i_1, j_1} \dots V_{i_Q, j_Q} V_{i'_1, j'_1}^* \dots V_{i'_Q, j'_Q}^* = \sum_{\sigma, \tau \in S_Q} \text{Wg}_D(\tau\sigma^{-1}) \delta_{i_1, j'_{\sigma(1)}} \dots \delta_{i_Q, j'_{\sigma(Q)}} \delta_{j_1, i'_{\tau(1)}} \dots \delta_{j_Q, i'_{\tau(Q)}}, \quad (9)$$

where $d\mu(V)$ denotes the unitary Haar measure.

A few comments are in order. The final result (8) contains Weingarten functions $\text{Wg}^{O(D)}(\cdot)$ for the orthogonal group $O(D)$, first introduced in the context of averaging over moments of orthogonal matrices in Ref. [132] (see Ref. [133] for a good review on these functions). Interestingly, the orthogonal Weingarten function $\text{Wg}^{O(D+1)}(\cdot)$ here is obtained by summing over a linear combination of the unitary Weingarten functions $\text{Wg}_D(\cdot)$. Although intriguing, this should not be surprising since the COE can be identified with the compact symmetric space $U(D)/O(D)$. However, the presence of $D + 1$ instead of D is indeed quite odd (as also noted by [122]) yet unimportant in our subsequent analysis. An exact

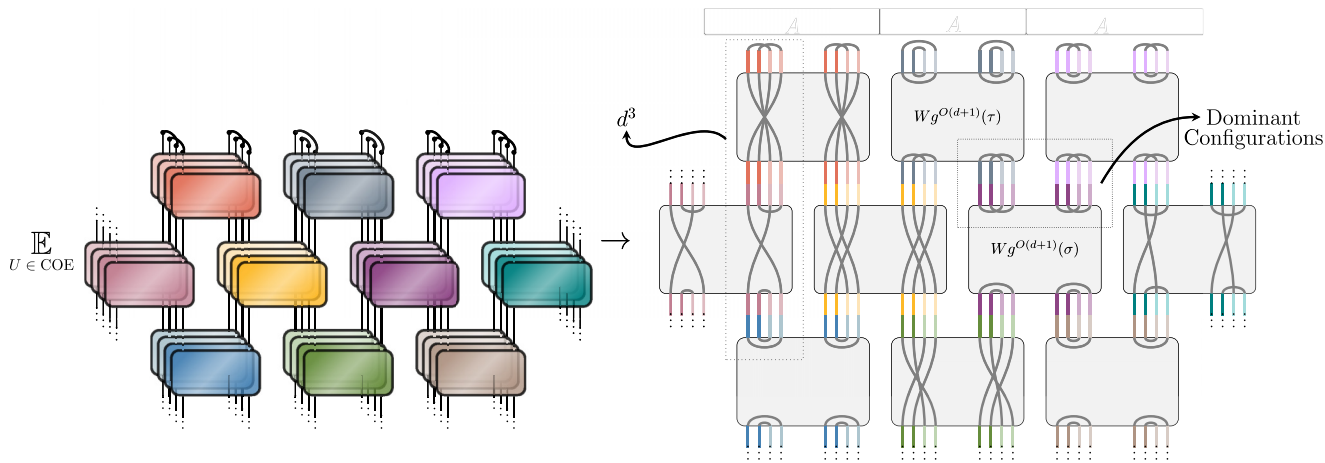


FIG. 4. Stat-mech model for local TR dynamics. Left: Replica circuits for local TR symmetric dynamics with $N = 2$. The numbering of the replicas from front to back is $(1, 2, 1^*, 2^*)$. Each of the gates within a replica are randomly sampled from the COE and are of the form $U = V^T V$. We further emphasize the randomness using different colors for nonidentical gates and vice versa. The conjugate replicas are colored with a lighter shade of the color corresponding to the unconjugated ones. The contraction at the top center depicts region A where the boundary conditions are g_{SWAP} . The contractions at the ends on top (\bar{A}) are represented with contractions $e \in S_N$. Right: A particular configuration of the statistical mechanics model derived from the averaging of the circuit on the left. The links are represented by the color of the respective gates on the left. The links of the conjugated replicas are emphasized using a lighter shade of the corresponding unconjugated replica links. The gray links pair conjugated links with the unconjugated ones based on the “spin” $\sigma \in S_{2N}$ at a given site. Link weights form loops which contribute as $d^{\#\text{loops}}$ to the partition function, while the vertex weights are given by $Wg^{O(d+1)}(\tau)$, $\tau \in S_{2N}$.

Fourier-type expansion for $Wg^{O(D+1)}(\tau)$ is given by [133]

$$Wg^{O(D)}(\tau) = \frac{2^N N!}{(2N)!} \sum_{\lambda \vdash N} \frac{f^{2\lambda}}{C'_\lambda(D)} \omega^\lambda(\tau), \quad (10)$$

where the sum is over integer partitions λ of N , such that $\lambda = (\lambda_1, \lambda_2, \dots)$ with $\lambda_1 \geq \lambda_2 \geq \dots \geq \lambda_l \in \mathbb{N}$, $\omega^\lambda(\tau)$ are zonal spherical functions (that can be expressed as a linear combination of the characters $\chi^{2\lambda}(\sigma)$ of $\sigma \in S_{2Q}$ associated with the irrep. λ), $f^{2\lambda}$ is the dimension of the irreducible representation associated with λ , and $C'(\lambda)(D) = \prod_{i=1}^{\lambda_i} \prod_{j=1}^{\lambda_i} (D + 2j - i - 1)$.

Probing Eq. (8) further, we observe a crucial distinction from the case of averaging over (unitary) Haar gates. Averaging over (unitary) Haar gates results in pairing the states in the input (output) legs of replicas with the input (output) legs of the conjugate replicas. However, averaging over the COE results in mixing between the input and output legs of conjugate replicas. In other words, the input legs of a replica can be paired with the outgoing legs of a conjugated replica. As a result of this, each leg of the ket can be paired with $2N$ legs of the bra, leading to a sum over $\tau \in S_{2N}$ in Eq. (8) instead of S_N in the standard Haar case. This also makes intuitive sense since averaging over a smaller set [in this case from $U(D) \rightarrow U(D)/O(D)$] would be expected to lead to a richer structure postaveraging.

Applying the result (8) for all gates in the circuit we can interpret Z_A as the partition function of a statistical mechanics model on a square lattice with the permutation in S_{2N} (“spins”) living on the vertices with vertex weights $Wg^{O(D+1)}(\tau)$ (see Fig. 4). The link weights on the other hand are calculated exactly like in the Haar case by contracting neighboring links and counting the number of loops. An example is shown in

the light-dotted rectangular box on the left side of the right panel under the letter \bar{A} in Fig. 4 where we count three loops resulting in the link weight d^3 . However, a difference here is that the loops could possibly be extended in space due to the input/output mixing mentioned earlier. Denoting the total number of loops in a configuration $\{g_v\}$ of permutations $g_v \in S_{2N}$ at the vertices of the square lattice by $l_{\{g_v\}}$, the bulk partition function for $Z_A \equiv Z_{\text{bulk}}$ can be written as

$$Z_{\text{bulk}} = \sum_{\{g_v \in S_{2N}\}} d^{l_{\{g_v\}}} \prod_{v \in \text{vertices}} Wg^{O(D+1)}(g_v). \quad (11)$$

Similar to the Haar case, the partition function has negative weights due to the negativity of $Wg^{O(D+1)}(\cdot)$ [133]. The boundary contributions to Z_A are as per Eqs. (4) and (5): Tracing over \bar{A} fixes the permutations in \bar{A} to be $e = \text{identity} \in S_N \subset S_{2N}$ and performing matrix multiplication of n copies (in each of the k replicas) corresponds to fixing the permutations in region A to be $g_{\text{SWAP}} \in S_N \subset S_{2N}$ [the notation $\tau \in S_N \subset S_{2N}$ denotes τ as a member of S_N embedded in S_{2N} . This embedding is given by grouping the legs $\{m, m'\}$ and permuting the resulting N objects as per S_N].

C. Stat-mech mapping for global TR symmetry

As discussed previously, we are interested in the case where we have global TR symmetry in addition to the local TR symmetry already present. As mentioned earlier, we refer to this model as the global TR symmetric model. Such a model requires that both the complete evolution and the local gates be written in the form $U = V^T V$. This can be implemented by adding a “mirror” to the existing local TR symmetric evolution as shown in Fig. 2(a). It will also hereon be useful

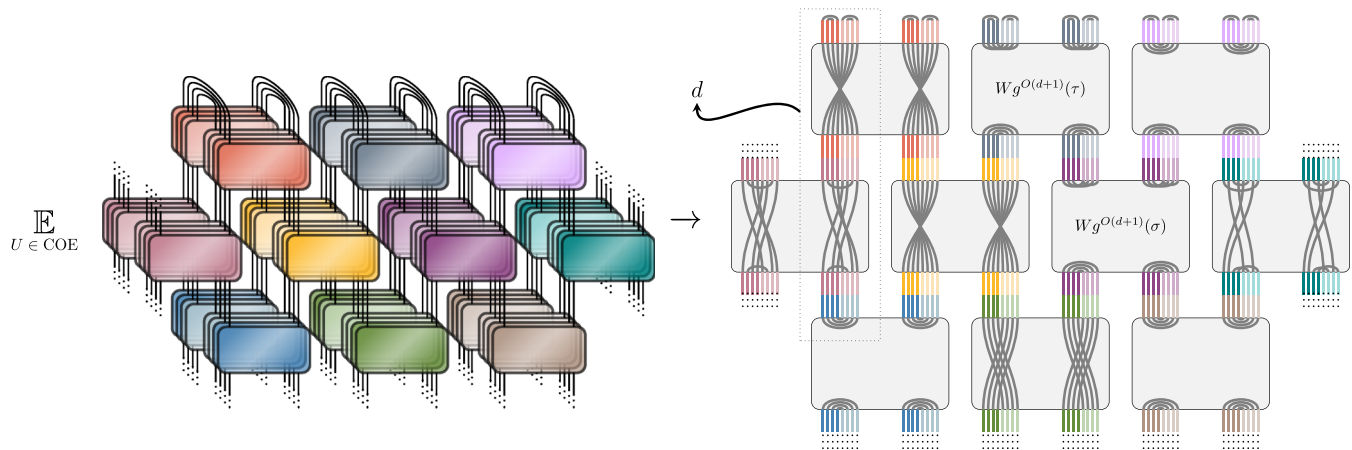


FIG. 5. Stat-mech model for global TR dynamics. Left: Replica circuits for global + local TR symmetric dynamics with $N = 2$. The numbering of the replicas from front to back is $(1, 2, 1^*, 2^*, \bar{2}^*, \bar{1}^*, \bar{2}, \bar{1})$, where we represent the mirrored replicas using a bar ($\bar{\cdot}$). Each of the gates within a replica are randomly sampled from the COE and are of the form $U = V^T V$. We further emphasize the randomness using different colors for nonidentical gates and vice versa. The conjugate replicas are colored with a lighter shade of the color corresponding to the unconjugated ones. The top boundary conditions pair each link with its mirrored counterpart. There are mixed boundary conditions at the bottom as explained in the main text (not shown here). Right: A particular configuration of the statistical mechanics model derived from the averaging of the circuit on the left. The links are represented by the color of the respective gates on the left. The links of the conjugated replicas are emphasized using a lighter shade of the corresponding unconjugated replica links. The gray links pair conjugated links with the unconjugated ones based on the “spin” $\sigma \in S_{4N}$ at a given site. Link weights form loops which contribute as $d^{\#\text{loops}}$ to the partition function while the vertex weights are given by $Wg^{O(d+1)}(\tau)$, $\tau \in S_{4N}$.

for us to refer to a mirror transformation at a site as the one that takes us from a site to its mirrored counterpart as per Fig. 2(a).

The stat-mech model requires averaging over nonlocally spaced gates, as depicted in Fig. 2(a). To address this, we can conceptualize a folded geometry where identical gates occupy the same space-time position [see Fig. 2(b)]. This simplifies the averaging process: We now have twice the number of replicas of U (or equivalently, twice the replicas of V) compared to the local case, and we must perform the average of $U^{\otimes 2N} \otimes U^{*\otimes 2N}$ at each gate location. The resulting expression is identical to Eq. (8), except we now have twice the number of gates at each site, and the sum runs over $\sigma \in S_{4N}$ instead of S_{2N} . This is because we have $2N$ replicas as before due to N kets and N bras. In addition, for each of the $2N$ replicas, we have a mirrored counterpart leading to $4N$ replicas in total. The emergent statistical mechanics model is illustrated in Fig. 5. Here, the link weights are determined by counting the number of (possibly extended) loops, and the vertex weights are given by $Wg^{O(D+1)}(\tau)$ with $\tau \in S_{4N}$.

The folded geometry begets several peculiarities to the global TR model. In the folded geometry, the transfer matrix of the corresponding statistical mechanics model can be interpreted as a superoperator that acts on a quantum channel and returns a quantum channel. Indeed, the “initial state” of this folded evolution is a quantum channel that maps initial to final state in the original quantum evolution, and the “seam” [at the top of Fig. 2(b)] at the final step of the folded evolution can be interpreted as the identity quantum channel.

Second, we note that each space-time point in this stat-mech model corresponds to two different instances in real-time evolution. Consequently, any operation performed in the stat-mech model will correspond to the same operation applied at two points related by a mirror transformation in the

real-time circuit. Furthermore, in the stat-mech model, “time” can be considered the vertical distance from the bottom or top end of the model in Fig. 5, which does not correspond to time in the actual circuit dynamics. The implications of these differences become evident when calculating the anisotropy factor, as discussed in Appendix B, where we outline a protocol to numerically extract correlation functions in this stat-mech model.

Another noteworthy difference from local TR due to the folded geometry are the boundary conditions. Here, we have mixed boundary conditions at the bottom because the initial and final states of the real-time evolution correspond to the same location in the stat-mech model. At each gate, half the links have free boundary conditions due to the freedom in the choice of the initial state, whereas the other half have their permutation fixed as $g_{\text{SWAP}}(e)$ in $A(\bar{A})$, respectively. At the seam (top), the boundary conditions are fixed by pairing both bra and ket in each replica with their corresponding mirrored counterpart in accordance with the mirror symmetry (see Fig. 5).

IV. APPLICATION: MIPT IN MONITORED TR-INVARIANT SYSTEMS

Random quantum circuits and their stat-mech mappings have proven invaluable in addressing various dynamical questions in quantum many-body systems [93,94]. These mappings have been successfully applied to study entanglement growth [8,9], operator spreading hydrodynamics [13], MIPTs [102,103], error correction [134], and the complexity of classical computations [135]. In this work, we explore the application of the aforementioned stat-mech models for the study of TR-symmetric MIPTs. We choose MIPTs as

our focus due to their versatility in applications and interpretations [16–19], making them an ideal starting point for demonstrating the utility of our stat-mech models. Like in the previous section, we give an overview of how the previously derived stat-mech models are altered once we include measurements for the local TR case followed by the global TR case. We then discuss the symmetry properties of these models and end by discussing some analytic results in the limit of large onsite Hilbert space dimension d .

A. MIPT setup

The basic setup is identical to the one in Sec. III A. We consider a brickwork random quantum circuit with gates being sampled from the COE. Such a circuit represents discrete time dynamics on a qudit spin chain of length L with Hilbert space dimension d at each site. In addition, we include projective measurements at every time step with a probability p on each qudit. We define a single realization of a circuit to be an instance of randomly picked COE gates and measurement locations. Starting with an initial state $\rho_0 := |\psi_0\rangle\langle\psi_0|$, one can then write the overall dynamics of a realization as a quantum trajectory $\rho_{\mathbf{m}} = K_{\mathbf{m}}\rho_0 K_{\mathbf{m}}^\dagger$. Here, we use \mathbf{m} for the list of measurement outcomes and $K_{\mathbf{m}}$ for the Kraus operators that contain unitary gates and projective measurements, with $K_{\mathbf{m}}$ satisfying the usual Kraus relation $\sum_{\mathbf{m}} K_{\mathbf{m}}^\dagger K_{\mathbf{m}} = \mathbb{I}$.

Our goal is to study the dynamics of the above setup. In particular, we probe the universal features of the dynamics using the n^{th} Rényi entanglement $S_{n,A}$ entropy [Eq. (1)]. Without the measurements, it is well known that the final steady state of a typical circuit has a volume law with $S_{n,A} \sim L$ in any given subsystem of size L . Such scaling behavior is consistent with the Eigenstate Thermalization Hypothesis (ETH) and is likewise observed in the TR symmetric models investigated in this work (see Secs. IV D and V for analytic and numerical evidence, respectively). The measurements inhibit this growth of entanglement and there is a critical measurement rate p_c above which the steady state exhibits area-law scaling $S_{n,A} \sim \mathcal{O}(1)$. This is indeed the measurement-induced phase transition. It is crucial to note that this transition takes place in the nature of the quantum trajectories $\rho_{\mathbf{m}}$ where the experimentalist keeps track of the measurement outcomes \mathbf{m} . The transition is invisible in the measurement averaged density matrix, such as in the case of decoherence. Consequently, we first evaluate properties of a given trajectory $\rho_{\mathbf{m}}$ and only then average over the gates, measurement outcomes, and locations.

Following Ref. [47], we use the notation $\mathbb{E}_U(\cdot)$, $\mathbb{E}_X(\cdot)$, and $\sum_{\mathcal{M}(\mathbf{X})}(\cdot)$ to denote averaging over COE gates, measurement locations, and over the measurement outcomes at a given set of locations \mathbf{X} , respectively. With a slight abuse of notation, we will also sometimes combine the average over the set $\{\mathbf{X}, \mathcal{M}(\mathbf{X})\}$ as $\sum_{\mathbf{m}} p_{\mathbf{m}}$. The average Rényi entanglement entropy we aim to compute can then be written as

$$\bar{S}_{n,A} = \mathbb{E}_U \sum_{\mathbf{m}} \left\{ p_{\mathbf{m}} \times \frac{1}{1-n} \ln \left[\frac{\text{tr}(\rho_{A,\mathbf{m}}^n)}{\text{tr}(\rho_{\mathbf{m}})^n} \right] \right\}, \quad (12)$$

where we weight each trajectory $\rho_{\mathbf{m}}$ with its corresponding Born probability $p_{\mathbf{m}} = \text{Tr}(\rho_{\mathbf{m}})$. The computation of the above average can be done using the Replica trick as shown in

Refs. [9,47,101–103] using Eq. (2) as

$$\bar{S}_{n,A} = \frac{n}{1-n} \lim_{N \rightarrow 0} \mathbb{E}_X \left[\frac{Z_A(\mathbf{X}) - Z_0(\mathbf{X})}{N} \right], \quad (13)$$

where

$$Z_A(\mathbf{X}) = \mathbb{E}_U \sum_{\mathcal{M}(\mathbf{X})} \left[\text{Tr} \left\{ (K_{\mathbf{m}}|\psi\rangle\langle\psi|K_{\mathbf{m}}^\dagger)^{\otimes(N+1)} \mathcal{S}_{n,A}^{\otimes k} \right\} \right], \quad (14)$$

$$Z_0(\mathbf{X}) = \mathbb{E}_U \sum_{\mathcal{M}(\mathbf{X})} \left[\text{Tr} \left\{ (K_{\mathbf{m}}|\psi\rangle\langle\psi|K_{\mathbf{m}}^\dagger)^{\otimes(N+1)} \right\} \right], \quad (15)$$

similar to Eq. (3). $Z_{A,0}(\mathbf{X})$ are identical in the bulk and differ in their boundary conditions being $S_{n,A}^k$ and \mathbb{I} , respectively. $N = nk$ is the number of replicas where replicas and the additional replica have entered by absorbing the $p_{\mathbf{m}}$ factor in Eq. (12) as $\text{Tr}(\rho_{\mathbf{m}})$. Finally, note that we do not include the average over the measurement locations \mathbf{X} in the above partition functions. This is because the statistical mechanics model for the MIPT will also have nonlocal weights that depend on \mathbf{X} , similar to the case with $p = 0$ (no measurements) discussed in the previous section.

B. Boltzmann weights

1. Local TR symmetric model

In order to obtain the statistical mechanics model, we need to evaluate the combination $\mathbb{E}_U \sum_{\mathcal{M}(\mathbf{X})} K_{\mathbf{m}}^{\otimes(N+1)} \otimes K_{\mathbf{m}}^{*\otimes(N+1)}$ from Eqs. (14) and (15). This average can be decomposed into separate averages: \mathbb{E}_U over the COE gates and $\sum_{\mathcal{M}(\mathbf{X})}$ over the measurement outcomes, which only involve the projection operators $P_i := |i\rangle\langle i|$; $i \in \{1, \dots, d\}$ in the TR-invariant basis. The gate averaging \mathbb{E}_U has already been discussed in Eqs. (6)–(8) and remains unchanged, resulting in the model as shown in Fig. 4. In addition to this, we have projection operators at the locations \mathbf{X} that freeze the links in all the replicas at all $X \in \mathbf{X}$ to the measurement outcome $\mathcal{M}(X)$, resulting in a factor of 1 in the partition function (due to $\text{tr} M^\dagger M$, where M is the measurement operator that projects onto the state $|\mathcal{M}(X)\rangle$). As per the stat-mech model in Fig. 4, the measurement at point X will consequently fix all the links that are part of the loops containing the links at X to the same outcome $\mathcal{M}(X)$. Therefore, any further measurement made at another part of the loops going through X , say X' , will only contribute when $\mathcal{M}(X) = \mathcal{M}(X')$. Performing the summation $\sum_{\mathcal{M}(X)}$ will then result in a factor of d corresponding to the set of loops that pass through X .

The statistical mechanics model for the TR-invariant MIPT can then be summarized as follows: We have a square lattice with permutation degrees of freedom σ living on the vertices with vertex weights $\text{Wg}^{O(D+1)}(\sigma)$, exactly like in the $p = 0$ case. The unmeasured link weights are calculated by contracting neighboring gates and counting the number of loops (assuming every link in the loop is unmeasured), with each loop contributing a factor of d . If a measurement is made at a given X , all the loops that contain any of the $2(N+1)$ links at X reduce to a total factor of d . Further measurements made at any other location containing links that form these frozen loops do not contribute. Denoting, for every configuration $\{g_v\}$ of permutations at the vertices of the square lattice, the total number of loops that contain all unmeasured links by $l_{\{g_v\}}(\mathbf{X})$

and the total number of measurement locations that do not have common loops by $m_{\{g_v\}}(\mathbf{X})$, the bulk partition function for $Z_{A,0} \equiv Z_{\text{bulk}}(\mathbf{X})$ is given by

$$Z_{\text{bulk}}(\mathbf{X}) = \sum_{\{g_v \in S_{2N}\}} d^{[l_{\{g_v\}}(\mathbf{X}) + m_{\{g_v\}}(\mathbf{X})]} \prod_{v \in \text{vertices}} W_g^{O(D+1)}(g_v). \quad (16)$$

The boundary conditions of Z_A are fixed as per Eqs. (4) and (5), whereas the boundary conditions for Z_0 are $e \in S_{N+1} \subset S_{2(N+1)}$ everywhere on the boundary.

We find a volume law to area law transition for this model at $p_c \approx 0.15$ (see numerical data in Fig. 8 and corresponding Sec. V). We delay the discussion of the critical properties and analytic results in the large d limit to later Secs. IV C and turn to discussing the MIPT stat-mech model for when the global TR symmetry is added.

2. Global TR symmetric model

The global TR symmetric $p = 0$ dynamics is modeled by the circuit in Fig. 2(a). As we shift p away from 0, we immediately disrupt the mirror symmetry essential for global TR dynamics, given the random nature of measurements. To preserve global TR, we must therefore implement measurements that respect the mirror symmetry. This means that for every measurement made at a specific space-time point in the first half of the evolution, a corresponding forced measurement must be made at its mirrored counterpart. Furthermore, we must also postselect the outcomes in the mirrored half to match those in the first half of the evolution. This is a stringent requirement and we investigate later on whether it is possible to relax this.

Due to postselection of measurements, the resultant stat-mech model does not follow directly from Eqs. (14) and (15), since for the Born probability we now have in general $\text{tr}(\rho_m) \neq p_m$, whereas there was an equality in the local TR symmetric case. This is because ρ_m is the state after the complete global TR symmetric evolution whereas p_m is calculated only from the first half of the evolution. Denoting the full evolution as $O_m = K_m^T K_m$ where K_m is the first half of the full evolution, one can then rewrite Eqs. (14) and (15) for the global TR symmetric model as

$$Z_A(\mathbf{X}) = \mathbb{E}_U \sum_{\mathcal{M}(\mathbf{X})} [\text{Tr}(O_m |\psi\rangle \langle \psi| O_m^\dagger)^{\otimes N} S_{n,A}^{\otimes k} \times \text{Tr}(K_m |\psi\rangle \langle \psi| K_m^\dagger)], \quad (17)$$

$$Z_0(\mathbf{X}) = \mathbb{E}_U \sum_{\mathcal{M}(\mathbf{X})} [\text{Tr}(O_m |\psi\rangle \langle \psi| O_m^\dagger)^{\otimes N} \times \text{Tr}(K_m |\psi\rangle \langle \psi| K_m^\dagger)], \quad (18)$$

where $p_m = \text{Tr}(K_m |\psi\rangle \langle \psi| K_m^\dagger)$. The resultant stat-mech model can be developed step by step as follows: For $p = 0$, the stat-mech model is the one in Fig. 5 with $2N$ replicas. For $p \neq 0$, we need to make two changes to this model. First, we get an additional replica due to p_m resulting in a total of $2N + 1$ replicas, where the Born replica is not doubled because the trajectories are fixed in the second half of the evolution owing to the postselection of measurement outcomes. Second, given a set of measurement locations \mathbf{X} , one must reduce all the

loops that cross the $2(2N + 1) = 4N + 2$ links in $X \in \mathbf{X}$ to a factor of d (instead of just $2N + 1$ as in the local model). The reasoning for this is the same as for the local TR MIPT model discussed previously. Measurements freeze the links at X (and now also its mirrored counterpart) in all the replicas to the same measurement outcome $\mathcal{M}(X)$, resulting in weight 1 in the partition function. We then sum over d possible measurement outcomes resulting in the total weight d in the partition function. Additionally, if there is a measurement at some other location X' involving the loops that cross through X , they only contribute when $\mathcal{M}(X) = \mathcal{M}(X')$. Finally, out of the $2N + 1$ total replicas, $2N$ replicas have the same boundary conditions as those for the model at $p = 0$: mixed boundary conditions at the bottom with half the legs being free and the other half being fixed as g_{SWAP} and e in regions A and \bar{A} , respectively, while the boundary conditions at the ‘‘seam’’ (on the top) are fixed by pairing both the bra and ket in each replica with their mirrored counterparts. The last Born-probability replica has e boundary conditions at the top and free boundary conditions at the bottom.

We find that this model has an entanglement transition at a critical measurement probability of $p_c \approx 0.15$ as well (see numerical data in Fig. 8 and corresponding Sec. V). However, as we shall now discuss, the two models have different symmetry properties and fall into different universality classes.

We summarize and close this section by highlighting the folded formulation as the natural description of a TR-invariant circuit. As will be emphasized later in this paper, the global TR-invariant circuit is the only version of the circuit that in fact possesses TR invariance, and this version has a folded description. Therefore, by default, a (global) TR-invariant circuit can always be described in the folded formulation, and we may consider this the defining property of a TR-invariant circuit. As mentioned (and as will be stressed again later), a global (or ‘‘strong’’) version of TR invariance enforces the presence of mirror symmetry in each quantum trajectory, and therefore the first half of the circuit evolution is the only independent evolution, completely determining the second half of the evolution. This is expressed in Eqs. (17) and (18) by writing the full evolution as $O_m = K_m^T K_m$. As visualized in Figs. 2 and 5, we can think of the evolution of the (global) TR-invariant circuit as acting on a doubled Hilbert space for each, the ‘‘ket’’ as well as the ‘‘bra’’ evolution; the doubling corresponds to the tensor product of Hilbert spaces associated with the first and second half of the evolution (i.e., of the two mirrored halves). Written out in terms of the vectorization of the density matrix $\rho_t = |\psi_t\rangle \langle \psi_t| \leftrightarrow |\rho_t\rangle\rangle = \sum_{i,i^*} \psi_i(t) \psi_{i^*}^*(t) |i, i^*\rangle\rangle$, Sec. III A (second paragraph), Fig. 5 reads in the presence of measurements ($t \geq 0$)

$$\begin{aligned} \langle\langle \text{Seam} | [(K_m \otimes K_m^*) \otimes (K_m \otimes K_m^*)] | \rho_{-t} \rangle\rangle \otimes |j, j^*\rangle\rangle &= \\ = \langle\langle j, j^* | [(K_m^T K_m) \otimes (K_m^{*T} K_m^*)] | \rho_{-t} \rangle\rangle &= \langle\langle j, j^* | \rho_{+t} \rangle\rangle, \end{aligned} \quad (19)$$

where the seam corresponds to the state

$$\langle\langle \text{Seam} | := \sum_{k,k^*} \langle\langle i, k^* | \otimes \langle\langle i, k^* |. \quad (20)$$

The action in the first line of Eq. (19) on the seam [Eq. (20)] as the ‘‘initial state’’ from the left with the evolution

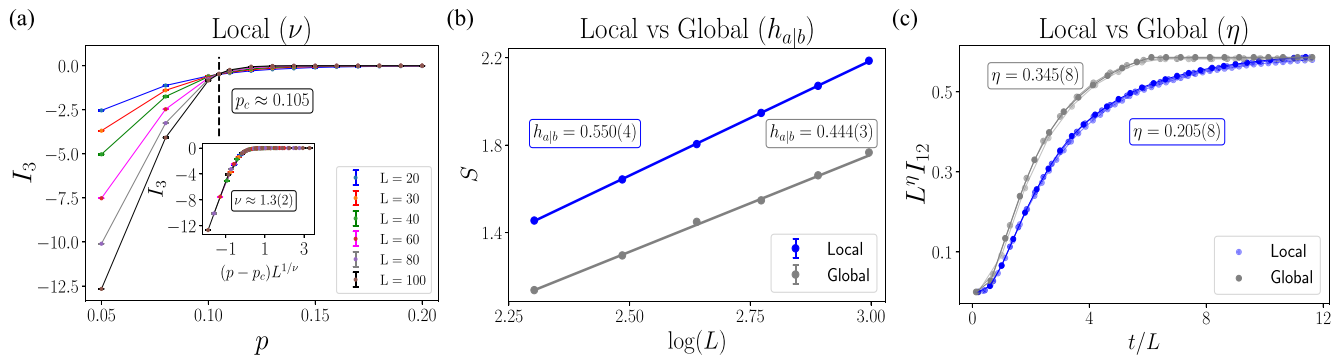


FIG. 6. TR-invariant Clifford numerics: (a) I_3 vs p . We perform finite-size scaling of I_3 to obtain the critical point $p_c \approx 0.105$ and correlation length exponent $\nu \approx 1.3(2)$ (plotted in the inset) for the local time-reversal model. We consider sizes $L = 20, 30, 40, 60, 80, 100$, and average each data point over 50 000 samples. (b) S vs L ; the bipartite entanglement entropy between two halves A and \bar{A} stays logarithmic ($\sim 2h_{a|b} \ln(L)$) at the critical point p_c ($p = 0.105$). We obtain the universal prefactor of \ln at criticality from the linear fit between S and $\ln(L)$. The blue and gray lines denote local and global, where the boundary exponent $h_{a|b} \approx 0.550(4)$ and $0.444(3)$ for local and global models, respectively. Clearly, the values differ and confirm different universality classes of local and global. (c) $I_{12}(t, L)$ vs t/L ; the dynamical scaling of space separated correlators $I_{12}(t, L)$ gives the bulk exponent η . We note a clear collapse and obtain bulk exponents $\eta = 0.205(8)$ and $0.345(8)$ for Local and Global models, respectively. Clearly, this again differs for the respective time-reversal models. We average each data over 100 000 samples and show collapse for sizes $L = 10, 14$, and 16 in shades of blue and gray for Local and Global models, respectively.

operator $[(K_m \otimes K_m^*) \otimes (K_m \otimes K_m^*)]$ of the folded circuit can be viewed as providing a definition of the (global) TR-invariant circuit on the doubled Hilbert space by an amount of time $\mathbf{t} = t \geq 0$ (half the total time $2t$). It has a “built-in” $Z_2 \times Z_2$ symmetry in every quantum trajectory, exchanging the two mirrored halves of the folded circuit independently in the evolution of the “ket” ($K_m \otimes K_m$) and of the “bra” ($K_m^* \otimes K_m^*$), which represents the “built-in” TR symmetry of the folded formulation. [As will be described in Sec. IV C 2, this will lead to a characteristic $H_N \times H_N$ symmetry of the statistical mechanics model of the (global) TR-invariant circuit.] For the so-described circuit, Eq. (19) expresses the statements in the last three paragraphs of Sec. III C, when measurements are present. Clearly, in the folded formulation, the special postselection requirement for the measurement outcomes in the second (mirrored) half of the evolution to match precisely those of the first half (as mentioned in the first paragraph of Sec. IV B 2) is simply replaced by working with the second tensor power $(K_m \otimes K_m^*) \otimes (K_m \otimes K_m^*)$ of the evolution operator of the first half of the circuit ($K_m \otimes K_m^*$). Since the calculation of averages of tensor powers of the circuit evolution operator (of the type mentioned, e.g., in the first sentence of Sec. IV B 1) is already a necessary ingredient for formulating observables relevant for the circuit dynamics, the additional doubling of the tensor power in the folded circuit corresponds, conceptually, to no additional feature or ingredient, or “postselection” effort. (But this doubling has impact on symmetry of the statistical mechanics model, as mentioned and discussed in Sec. IV C 2).

Finally, we note that the folded formulation of the (global) TR circuit makes the emergence of conformal symmetry at the transition that requires the ability to exchange the roles of circuit space and time, more understandable, which would be more difficult to formulate in the postselected, not-folded description of the same circuit. Similarly, the folded

formulation also exhibits a link between global TR-invariant circuits and circuits possessing spatial reflection symmetry $x \rightarrow -x$ in every quantum trajectory.

C. Universality and symmetry

1. Local TR model

The symmetry groups of stat-mech models corresponding to MIPTs dictate their critical properties. In this section, we examine the symmetry properties of both the MIPT stat-mech models with TR symmetries discussed in Sec. IV B. In the following, we use lower case n when referring to groups more broadly (with no direct reference to MIPT or the stat-mech model in general) and reserve uppercase N for the number of replicas.

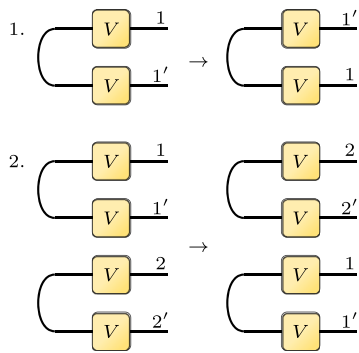
A key group that emerges in the study of these models’ symmetries is the hyperoctahedral group H_n , a subgroup of S_{2n} . Formally, H_n is introduced by considering the labeling of $2n$ objects by $\{1, 1', 2, 2', \dots, n, n'\}$. (Here, we use a notation as in Fig. 6, where l and l' denote, e.g., the output and the input leg of the gate in replica number l .) H_n is then defined as the set of

- (1) Single transpositions $(l l')$ for $1 \leq l \leq n$,
- (2) Double transpositions $(l m)(l' m')$ for $1 \leq l, m \leq n$.

In our problem, H_N can be understood as being generated by the operations that permute replicas (giving the $S_N \subset H_N$ subgroup of H_N) and operations that permute the input/output legs of gates within each replica. [The cardinality of H_N can thus be verified to be $2^N N!$. There are $N!$ permutations of the group S_N , and each permutation has 2 internal permutations from switching the legs of the symmetric gate, resulting in $2^N N!$ operations.]

These operations indeed keep Eqs. (6)–(8) invariant, even before averaging step [Eq. (7)]. H_N generators can also be seen

graphically as being implemented by



We emphasize that while the latter (double transposition) is the standard replica permutation symmetry that exists even for the unsymmetric Haar case, the former (single transposition) is a manifestation of the symmetric structure imposed by time reversal.

It turns out that the vertex weights $\text{Wg}^{O(D+1)}(\tau)$ ($\tau \in S_{2N}$) are also symmetric under the action of the group $H_N \times H_N$ [122,136]. An intuitive way to see this is to first note that the contraction block in Eq. (8) counts the number of loops. There exist two operations that keep the number of loops in this block constant. These are as follows:

(1) Exchanging any two consecutive set of legs that are connected by the external black loops originating from the forced contraction of U^T and U .

(2) Transformations $\sigma \in S_N \subset S_{2N}$ that permute the pairs of these consecutive legs between the ket (yellow) and the bra (blue) side.

The above transformations can be directly compared to the two generators of H_N outlined earlier, leading us to conclude that the contractions and therefore $\text{Wg}^{O(D+1)}(\tau)$ are symmetric under $H_N \times H_N$.

Consequently, in the local TR MIPT model, the Weingarten functions are symmetric under $H_{N+1} \times H_{N+1}$, where we recall that the additional replica is due to the Born probability factor. While in Clifford and Haar ensemble, the link weights obey the symmetry of the respective Weingarten functions [104,137], this does not hold true for the link weights of the local TR model as we shall now explain. We first note that the link weights are at minimum symmetric under $S_{N+1} \times S_{N+1}$ since this symmetry exists microscopically for each circuit and originates from invariance under exchanging the replica copies of the circuit in the bra and ket, respectively. This symmetry is also trivially respected by measurements, as they contribute in the form of scalars to the partition function and admit no change when exchanging replicas. Since we know that the vertex weights (i.e., the Weingarten functions) are symmetric under $H_{N+1} \times H_{N+1}$, we need to only check whether the link weights are symmetric under permutations that are not in $S_{N+1} \times S_{N+1}$ but in $H_{N+1} \times H_{N+1}$ in order to obtain the symmetry group of the full model. The permutations of this type are generated by the transpositions ($l l'$), $1 \leq l \leq (N+1)$ listed earlier, which exchange the input and output legs at each gate in both the bra and the ket. In Fig. 4, these types of transformations generically involve “tearing” and re-joining loops, which does not generally preserve the number of loops. Consequently, the symmetry group

for the local TR MIPT model is $S_{N+1} \times S_{N+1}$, placing it in the same universality class as that of the Haar MIPT.

One might have intuitively expected a larger symmetry group for ensemble-averaged local TR symmetric dynamics, given the richer structure emerging after averaging as suggested by Eq. (8). An example of this phenomenon is the Clifford ensemble, where the symmetry group of the MIPT stat-mech model is the orthogonal stochastic group $O_{N+1}(p) \times O_{N+1}(p)$, which contains the subgroup $S_{N+1} \times S_{N+1}$, with $d = p^L$, where p is prime and L represents the length of the qudit chain [104,137]. In fact, for local TR dynamics, we do indeed have an $H_{N+1} \times H_{N+1} \supset S_{N+1} \times S_{N+1}$ symmetry at the level of gate averaging. This occurs because exchanging the input and output legs ($(l l')$, $1 \leq l \leq (N+1)$) leaves Eq. (6) invariant. However, this symmetry is lost in the statistical mechanics model once the averaging is applied globally to the entire circuit, reducing the symmetry back to $S_{N+1} \times S_{N+1}$.

In summary, the hyperoctahedral group H_n is a symmetry of the n -copy COE gate averaging Eqs. (6)–(8) and associated with the TR symmetry in the quantum problem. However, when we evaluate the stat-mech model for the local TR MIPT using results from COE gate averaging, the symmetry is reduced to the permutation subgroup $S_{N+1} \subset H_{N+1}$. This results in an overall symmetry group of $S_{N+1} \times S_{N+1}$ for the local TR model—just like in the non-TR-invariant Haar case.

2. Global TR model(s)

Recall that the major change in going from local to the global TR model is to change the number of replicas from $N+1$ to $2N+1$. Consequently, the stat-mech model has $S_{2N+1} \times S_{2N+1}$ symmetry generated by exchanging any two replica copies. [Similar to the local case, the Weingarten functions $\text{Wg}^{O(D+1)}(\tau)$ are now symmetric under $H_{2N+1} \times H_{2N+1}$ but the link weights limit the symmetry to $S_{2N+1} \times S_{2N+1} \subset H_{2N+1} \times H_{2N+1}$.] Measurements also respect this symmetry since they force *all* the $2N+1$ replica links (in both the bra and the ket) to have the same state thereby making them symmetric under the permutations in $S_{2N+1} \times S_{2N+1}$. Therefore, the full stat-mech model for this version of the MIPT is symmetric under $S_{2N+1} \times S_{2N+1}$ in the bulk.

While there is an enlarged permutation symmetry in the bulk, this symmetry is broken down at the top boundary, see symmetry discussion at the end of Sec. IV B 2. This is because the seam breaks $S_{2N+1} \times S_{2N+1}$ down to $H_N \times H_N \subset S_{2N+1} \times S_{2N+1}$. One can check this by considering the N -fold replicated “seam” state from Eq. (20) and re-writing it as

$$\begin{aligned} \langle\langle \text{Seam} \rangle\rangle^{\otimes N} &= \sum_{\vec{i}, \vec{k}^*} \langle\langle i_1, k_1^*, i_2, k_2, \dots, i_N, k_N^* \rangle\rangle \otimes \\ &\langle\langle i_1, k_1^*, i_2, k_2^*, \dots, i_N, k_N^* \rangle\rangle, \end{aligned} \quad (21)$$

where $\vec{i}, \vec{k}^* = (i_1, i_2, \dots, i_N), (k_1, k_2, \dots, k_N)$. The state above has a $Z_2 \times Z_2$ symmetry built in, implemented by exchanging mirrored pair $i_n \leftrightarrow i_n, 1 \leq n \leq N$ (and correspondingly for k^*). It is additionally invariant under the transpositions that exchange the pairs $(i_n, i_n) \leftrightarrow (i_m, i_m), 1 \leq m, n \leq N$ (similarly for k^*), where the two i_n 's correspond to mirrored partners

(using the notation introduced in the second paragraph of Sec. IV C 1). These are precisely the generators of $H_N \times H_N$ as explained at the beginning of Sec. IV C 1. This fact can also be seen graphically from Fig. 5. Specifically, if the replicas are labeled as $(1, 2, \dots, N, \bar{1}, \bar{2}, \dots, \bar{N})$, where the overbar denotes the mirrored counterpart of the replica as in Fig. 5, the relevant H_N subgroup that keeps the seam intact is generated by single transpositions $(l \bar{l})$ with $1 \leq l \leq N$, and double transpositions $(l m)(\bar{l} \bar{m})$ with $1 \leq l, m \leq N$. The single transpositions represent the additional nonpermutation symmetry introduced by TR. Additionally, note that the Born-probability replica is excluded when discussing the H_N subgroup, as it does not double and therefore does not have a mirrored partner.

While the local TR MIPT falls into the universality class of the prototypical Haar MIPT due to its full enlarged permutation symmetry $S_{2N+1} \times S_{2N+1}$, global TR gives us a universality class of dynamics. Note that this would have been the case even if we did not have local TR dynamics. This is because the permutation symmetry S_{2N+1} emerges from the exchange of replicas—whose number increases from $N+1$ to $2N+1$ due to the mirrored structure enforced by global TR—not from the presence of local TR symmetry. This establishes a key result of our work, namely, that ensemble averaged global TR symmetric monitored dynamics (with measurements postselected to satisfy TR invariance in a “strong” way, i.e., in every quantum trajectory) represents a universality class of dynamics.

The experimental overhead of postselecting in the global TR model is in addition to the already exponential overhead of postselecting to observe MIPTs, a problem famously termed the “postselection problem” [97]. Although there are several approaches to overcome this problem [18,27,95,138–141], one would like to reduce the extent to which there is postselection. This leads us to investigate the universality class of a model that mirrors the gates and the measurement locations but not the measurement outcomes. We shall subsequently refer to this model as the “global TR symmetric model without postselection,” although it is important to keep in mind that global TR symmetry is microscopically broken when we do not postselect in the second half. A reason one can still however hope for the dynamics to fall in the same universality class as global TR dynamics is due to averaging occasionally giving rise to emergent symmetries. For example, Haar random circuits break translational symmetry yet the resultant stat-mech model is indeed invariant under translations. A similar emergence could potentially arise in the non-postselected case, where one might hope that some notion of “average TR invariance” emerges upon averaging over measurement outcomes.

It is easy to check whether such emergence occurs in this case. We consider the stat-mech model for the case with microscopic global TR symmetry and examine how the symmetries change when we do not post-select in the second half. Note that the measurements in the postselected case respect $S_{2N+1} \times S_{2N+1}$ as explained earlier. In the non-postselected case however, only half the number $(N+1)$ of links in both the bra and ket are required to agree upon measurement since the latter half of the evolution now has a different trajectory. Consequently, any transformation that permutes between the

two sets of $(N+1)$ links will generally not be a symmetry of the stat-mech model. Therefore, this model also has $S_{N+1} \times S_{N+1}$ symmetry, just like the local TR symmetric case.

To summarize, we have established that while local TR monitored dynamics falls into the (unitary) Haar universality class, global TR dynamics (with postselected measurements) presents a universality class of dynamics. Here, we re-emphasize the crucial role of the stat-mech model in revealing this key distinction, which is central to our analysis. For example, a single replica gate average $\mathbb{E}_{U \in \text{COE}}(U^{\otimes N} \otimes U^{*\otimes N})$ [see Eqs. (6)–(8)] exhibits a different $H_N \times H_N \supset S_N \times S_N$ symmetry, obscuring this distinction and failing to capture the correct universal features of monitored TR dynamics. While previous works [123,124] have explored aspects of TR symmetry in random circuits, they do not address this particular distinction, which emerges only at the level of the full stat-mech model. Finally, although the symmetry properties are tractable, the stat-mech models [Eqs. (16) and (18)] are complicated due to their nonlocal link weights. The limit of large- d however drastically simplifies the Boltzmann weights allowing us to make predictions about the nature of the entanglement transition [47,103,104] as we shall now discuss.

D. $d \rightarrow \infty$ limit

We begin by considering the simpler local TR symmetric model (16). In the limit of infinite onsite Hilbert space dimension $d \rightarrow \infty$, the vertex weights of this stat-mech model simplify to [122]

$$\text{Wg}^{O(d^2+1)}(\tau) = d^{-2(N+1)} \delta_{\tau \in H_0} + \mathcal{O}(d^{-2N-6}), \quad (22)$$

where $\delta_{g \in H_{N+1}}$ is defined to be $= 1$ only when $\tau \in H_{N+1}$, but $= 0$ for any other elements $\tau \in S_{2(N+1)}$. This is based on the fact that the Weingarten function $\text{Wg}^{O(d^2+1)}(\tau)$ for $\tau \in S_{2(N+1)}$ is invariant under right and left multiplication of the argument τ by group elements of the subgroup $H_{N+1} \subset S_{2(N+1)}$ (as discussed, e.g., in the footnote in Sec. IV C 1; or see Refs. [122,133]). Therefore, the Weingarten function is constant on the double cosets of H_{N+1} in $S_{2(N+1)}$, and is only a function of the double cosets; the subgroup H_{N+1} is itself one of the double cosets, namely, the “identity double coset” $H_{N+1}eH_{N+1} = H_{N+1}$, where $e = \text{identity} \in S_{2(N+1)}$, labeled by the partition $\lambda = (1, 1, \dots, 1)$ [see Eq. (A1)]. Unlike in the cases of group-based ensembles like Haar and Clifford for which the Weingarten functions attain a maximum at a particular configuration (identity), the Weingarten functions here thus attain a maximum on an entire double-coset, which is the “identity double coset” $= H_{N+1}$.

As expected, we find that the $d \rightarrow \infty$ limit of this model mimics that of the Haar MIPT stat-mech model [103]. As we increase d , local loops begin to dominate thereby gradually erasing the distinction between local TR and the Haar MIPT models. This happens because local loops tend to increase the total number of loops in the configuration increasing their overall probability as per Eq. (16). Locality implies we restrict to $S_{N+1} \subset H_{N+1}$ and the dominant configuration occurs when we have $g_v = g_{v'}$, where $\{g_v, g_{v'}\} \in S_{N+1} \subset H_{N+1}$, with v, v' labeling all possible neighboring vertices. Note that this configuration also maximizes the vertex weights according to Eq. (22).

An advantage of a local Haar-like configuration is that we can now perform the average $\mathbb{E}_{\mathbf{X}}$ exactly as in the Haar case giving local link weights [103]

$$W_p(g_v, g_{v'}) = pd + (1 - p)d^{N+1}\delta_{g_v, g_{v'}}. \quad (23)$$

Equations (22) and (23) collectively imply that the Boltzmann weights for the stat-mech model [Eq. (16)] reduce to those of the Potts model with $(N + 1)!$ colors [103]. In the replica limit $N \rightarrow 0$, we naturally obtain a percolation picture for this transition where we have clusters of aligned spins diluted by measurements with the transition occurring at $p_c = 1/2$ above which the number of clusters proliferates.

The large- d limit also allows us to take the replica limit [Eq. (13)] exactly and analytically realize the entanglement transition through the scaling of $\tilde{S}_{n,A}$. The argument here is same as that in Ref. [47], where it was given in the context of a global $U(1)$ symmetry. We briefly repeat it here for completeness. Equation (13) can be rewritten to express $\tilde{S}_{n,A}$ as a difference in free energies $\Delta F = F_A - F_0 = -\ln(Z_A/Z_0)$. In the limit $d \rightarrow \infty$, both Z_A and Z_0 have the same bulk configuration of aligned spins and only differ at the boundary with Z_0 having a uniform boundary and Z_A having a domain wall due to a different boundary condition (5) in region A. The ratio $Z_A/Z_0 = d^{(k+N)l_{\text{DW}}}$ (see Ref. [47]), where $l_{\text{DW}} = l_{\text{DW}}(\mathbf{X})$, is the number of unmeasured links the DW crosses. Since the free energy cost $\Delta F \gg 0$, the DW will minimize l_{DW} following a “minimal-cut” prescription. Finally, taking the replica limit gives $S_{n,A} = l_{\text{DW}}(\mathbf{X}) \ln d$, valid for all values of p . Averaging over \mathbf{X} , one finds that for values of $p < 1/2$, $l_{\text{DW}} \sim L_A$, where L_A is the length of the subsystem A. For $p > 1/2$ on the other hand, $l_{\text{DW}} \sim \mathcal{O}(1)$ with the transition occurring at $p_c = 1/2$ as predicted by percolation.

The above considerations do not change for the global TR scenario. The stat-mech model for the global TR MIPT has the same vertex and link weights (upto boundary conditions and difference in the number of replicas) due to which the large- d limit here also mimics the Haar case and maps to percolation, this time in the $N \rightarrow 0$ limit of the Potts model $S_{(2N+1)!}$. One might initially expect the entanglement entropy that was realized analytically in the replica limit to also change by a factor because of the change the number of links at each site as compared to Haar/local TR. However, the mixed boundary conditions for global TR imply that only half of the first $2N$ links at the bottom boundary contribute to the partition function. Additionally, the extra replica continues to have identity ($e \in S_{2(N+1)}$) boundary conditions. These facts combined lead to the replica limit being unchanged from the Haar/local TR case.

V. NUMERICS

In this section, we present numerical evidence supporting the claims made in this work using Haar and Clifford monitored circuits. While Haar-monitored circuits represent generic TR-invariant quantum dynamics, their Clifford counterparts—though belonging to a distinct universality class of “Clifford TR dynamics”—are efficiently simulable and thus provide additional support for our claims. Through these simulations, we demonstrate that the MIPT for global TR dynamics belongs to a universality class. In contrast, the

TABLE I. Critical exponents for the local and global time-reversal circuits at their respective critical point p_c . In particular, we extract the correlation length exponent ν , boundary scaling dimension h_{alb} , (typical) bulk exponent $\eta = 2x_1^{\text{lyp}}$, and dynamical exponent z for Clifford time-reversal circuits, and compute the effective central charge c_{eff} for the Haar time-reversal models.

Critical parameters	Time-reversal models		
	Local	Global ^a	Global
p_c (TR – Clifford)	0.105(1)	0.105(2)	0.120(3)
ν	1.3(2)	1.1(1)	1.0(3)
h_{alb}	0.550(4)	0.550(4)	0.444(3)
η	0.205(8)	0.215(6)	0.345(8)
z	1.06(8)	1.02(6)	1.00(9)
p_c (TR – Haar)	0.15	0.15	0.146
c_{eff}	0.26(3)	0.27(3)	0.38(5)

^aGlobal TR model without postselection in the second half.

MIPTs for local TR dynamics, as well as the non-postselected version of global TR, share the same universality class. Additionally, for both the Haar and Clifford cases, we find that the universality classes of the latter align with those of the Haar and Clifford random MIPTs without global symmetries.

A. Clifford TR numerics

The transition can be formulated using Clifford gates which respect time-reversal symmetry. To construct such a gate set, we select unitaries satisfying $U = U^T$ from the finite two-qubit Clifford group. There are a total of 340 such gates, where elements show up from all four Clifford classes (namely, Single qubit, swap, iswap, and cnot class) [142]. This indeed gives rise to nontrivial transition physics for Clifford time-reversal models. Moreover, the scalability allows to get precise estimates of universal exponents, which is further used to establish all claims made for universality classes of local and global time-reversal models.

We first obtain the critical point using standard MIPT order parameters such as tripartite mutual information I_3 (TMI) [16,28] and ancilla order parameter S_q [27]. We note a crossing and show a clear scaling of I_3 with $(p - p_c)L^{1/\nu}$ in Fig. 6(a) for the local time-reversal model. This gives both p_c and the correlation length exponent ν . Similar scaling law allows to extract these values for other models which we list in Table I. Note the values stay in agreement with the ancilla probe (not shown here). Now locating ourselves at p_c , we extract the standard boundary scaling dimension h_{alb} [24,66,104] and (typical) bulk exponent $\eta = 2x_1^{\text{lyp}}$ [16,27,28,46], from ln scaling of the bipartite entanglement entropy S and time dynamics of space separated (typical) correlators $I_{12}(t, L)$, respectively. In particular, we show there comparison for the local and the global model in Figs. 6(b) and 6(c). We go on computing similar exponents for the non-postselected global time-reversal model, denoted as Global*. The values extracted for all cases are summarized in Table I. The exponent values correctly identify that local and global belong to different universality classes, whereas both local and global* belong to the known Clifford universality class. Additionally, we note for all models the dynamical exponent z stays close to 1.0.

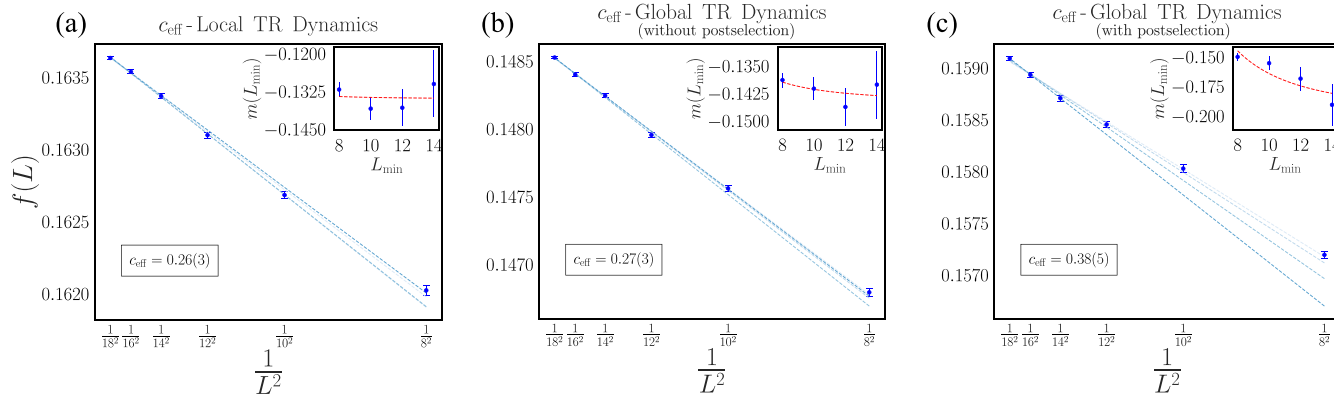


FIG. 7. Free energy density $f(L)$ vs $1/L^2$ for Haar TR models: The densities are plotted at respective p_c as per Fig. 8 for (a) local TR dynamics, (b) hlobal TR dynamics, and (c) global TR dynamics without postselection. The dotted lines indicate the linear fitting obtained using different L_{\min} . The inset shows resulting slopes $m_0(L_{\min})$ vs L_{\min} , where we omit the data points for $L < L_{\min}$. We fit the slopes to the curve $m_0(L) = a + b/L^2$, allowing us to extract c_{eff} [see Eq. (25)]. Each data point in the above plots is a result of averaging over more than 4×10^4 circuits.

B. Haar TR numerics

For the Haar case, we start by locating p_c using TMI as a probe just like in the Clifford case. We find that the TMI records are remarkably similar across the three variants (see Fig. 8). Given such close entropy records, we anticipate that the correlation length exponents ν and the prefactor of the logarithm for the Rényi entropy S_n at criticality (sometimes denoted by $\alpha(n)$ [28], not to be confused with the anisotropy factor α (Appendix B), and for the case $n = 1$ typically [24,66,104] by $\frac{1}{2} \times \alpha(1) = h_{ab}$) to be very similar across these models. Therefore, to effectively distinguish the universality classes of the Haar circuits, we focus on evaluating the effective central charge c_{eff} instead. This approach allows us to better characterize the critical properties between the Haar TR symmetric models that are not apparent from the TMI data alone.

1. Effective central charge (c_{eff})

Before we discuss our results for Haar TR models, it is first worth reviewing how the effective central charge c_{eff} is described. Our discussion closely follows Refs. [46, 66].

An alternate way to formulate the stat-mech models for these MIPTs is to think of each trajectory as a $(1+1)$ -dimensional statistical mechanics model with the partition function $Z_{\mathbf{m}} \equiv p_{\mathbf{m}}$. The trajectories altogether form an ensemble of statistical mechanics models with quenched disorder due to the measurements, and where we weigh each trajectory with $p_{\mathbf{m}}$. The quenched free energy F of the resultant stat-mech model can then be written as

$$F = - \sum_{\mathbf{m}} p_{\mathbf{m}} \ln p_{\mathbf{m}}, \tag{24}$$

where F is the quantity that we numerically calculate. Notably, the finite-size scaling of F is governed by conformal invariance. To understand this, we can consider the partition function of the stat-mech model as a replicated partition function $Z_{\mathbf{m}}^k = p_{\mathbf{m}}^k$, weighted with the Born probability $p_{\mathbf{m}}$. This gives us $\bar{Z}_k = \sum_{\mathbf{m}} p_{\mathbf{m}}^k p_{\mathbf{m}}$, which is precisely the form of the partition functions of the stat-mech models we have discussed earlier [143]. The corresponding annealed averaged free energy can be defined as $F_k = -\ln \bar{Z}_k$. Using the replica trick, one can recover $F = \lim_{k \rightarrow 0} \frac{dF_k}{dk}$. Since we know that F_k undergoes a second-order phase transition governed by

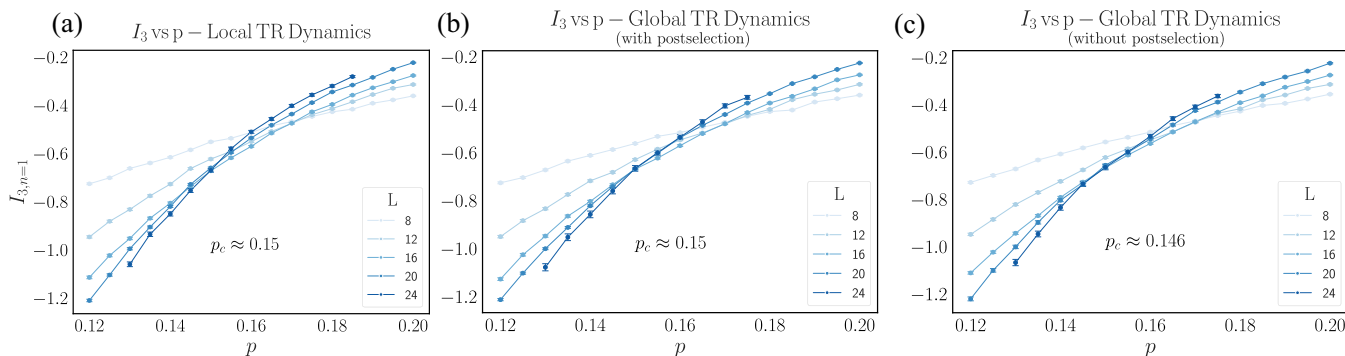


FIG. 8. Tripartite mutual information (TMI) vs p for $L = 8, 12, 16, 20, 24$ for Haar TR models. In all three cases, each point above is a result of averaging over 10 000 circuits for $L = 8, 12, 16, 20$ and 2000 circuits for $L = 24$. (a) Global TR with $p_c \approx 0.15$. (b) Local TR with $p_c \approx 0.15$. (c) Global TR without postselection with $p_c \approx 0.146$.

conformal invariance (with the replica limit coinciding with the MIPT of interest), F does too. More precisely, standard results in CFT imply that the bulk free energy density $f(L) = F/(\alpha tL)$ at criticality scales as

$$f(L) = f(L = \infty) - \frac{\pi c_{\text{eff}}}{6L^2} + \dots, \quad (25)$$

where we have considered a cylindrical geometry of circumference L , circuit depth t , and where α characterizes the asymmetry between space and time in our stat-mech model. Using the replica limit, the effective central charge above can be written as $c_{\text{eff}} = \lim_{k \rightarrow 0} \frac{dc(k)}{dk}$, where $c(k)$ is the central charge for the model defined by \bar{Z}^k . It is important to note that $c(k)$ itself is not the quantity of interest. This is because $\lim_{k \rightarrow 0} c(k) = 0$, due to the partition function \bar{Z}^k becoming trivial in this limit (i.e., $\lim_{k \rightarrow 0} \bar{Z}^k = 1$).

2. Results

Here, we present the results for the Haar TR circuits. The free energy calculations were performed following the procedure outlined in the supplemental material of Ref. [46]. The protocol for evaluating the anisotropy parameter for the local TR case is also the one used in Ref. [46]. However, for global TR-symmetric models, the protocol was modified to account for the two-to-one space-time correspondence between the circuit and the stat-mech model (see Fig. 5). Full details of this adjustment can be found in Appendix B.

The anisotropy values obtained are $\alpha_{\text{global}} = 0.61(8)$, $\alpha_{\text{global}^*} = 0.64(6)$, and $\alpha_{\text{local}} = 0.59(5)$. Figure 7 shows the free energy density results, where $f(L)$ is plotted against $1/L^2$. As expected, the behavior is linear in all cases. Using a double fitting procedure [46,66], we estimate $f^{\text{global}}(L) = -0.19(3) + \frac{3.42(1)}{L^2}$, $f^{\text{local}}(L) = -0.13(1) + \frac{0.20(2)}{L^2}$, and $f^{\text{global}^*}(L) = -0.14(3) + \frac{0.25(3)}{L^2}$.

We then compute the effective central charges using Eq. (25). For the local TR dynamics and global TR dynamics without postselection, the effective central charges indeed match that of Haar [$c_{\text{eff}} = 0.25(3)$], yielding $0.26(3)$ and $0.27(3)$, respectively. Furthermore, we find $c_{\text{eff}} = 0.38(5)$ for the global TR dynamics (with postselection), placing it in a different universality class as claimed earlier in this work.

VI. OUTLOOK

Our work explores TR symmetry in chaotic quantum systems through the framework of random quantum circuits. We distinguish between two types of TR symmetry in these circuits: local and global. Local TR symmetry requires each individual gate U to be symmetric ($U^T = U$), while global TR symmetry requires that the full evolution is of that form. We show that this amounts to picking gates from the COE. By averaging over moments of the COE, we then develop a replica stat-mech model generalizing the approach of Refs. [9,102,103]. This mapping could then be employed to probe ensemble-averaged values of observables such as Rényi entropies and characterize operator spreading through calculation of out-of-time-ordered correlators and other many-body quantum chaos metrics. As an example of application, we used this model to investigate MIPTs in moni-

tored TR-invariant quantum systems, where the measurements are performed in a TR-invariant basis.

Despite making measurements in the TR-invariant basis, our symmetry analysis reveals that the local TR-symmetric model shares the same $S_N \times S_N$ symmetry as the Haar stat-mech model (where N is the number of replicas), suggesting that they belong to the same universality class. In contrast, the global TR case, owing to the folded geometry of its stat-mech model (see Fig. 5), displays an enlarged replica permutation symmetry, placing it in a universality class. We find that this universality class is sensitive to the microscopic global TR symmetry. Specifically, not postselecting measurements while maintaining a globally symmetric structure for the unitary part (while also making measurements symmetrically in a TR basis) reverts the universality class back to that of Haar. In this sense, there is no emergent TR symmetry in the global TR stat-mech model when we do not postselect the outcomes in the second half of the time evolution. It is important to emphasize that the emergence of the universality class is driven primarily by TR symmetry in each individual trajectory of the ensemble, rather than by the spatial ordering of the circuit. In fact, it is TR symmetry that enforces the “mirrored” circuit structure (as discussed in Sec. II), and it is precisely this symmetry that gives rise to the universality class. More broadly, modifying the space-time ordering of a circuit does not inherently produce universality classes—unless such ordering is mandated by a symmetry, as is the case with TR here.

We present numerical evidence to substantiate the above claims by analyzing using both Haar and Clifford monitored circuits. Specifically, we observe that the Clifford variant and the Haar variant of the global TR symmetric model exhibit distinct critical exponents and effective central charges, respectively. In contrast, both the non-postselected global model and the local TR symmetric model, which share the same symmetries, are shown to have nearly identical critical exponents and effective central charges that differ from the global postselected case.

In this work, we have addressed arguably the simplest non-trivial case of time-reversal invariance where the time-reversal operator squares to plus the identity, $\mathcal{T}^2 = +1$ (“orthogonal symmetry class”). We expect additional space-time symmetries such as parity \mathcal{P} or charge conjugation \mathcal{C} , as well as chiral symmetry $\mathcal{T} \cdot \mathcal{C}$, to alter the universality of the dynamics. Details of such extensions, particularly to the case where $\mathcal{T}^2 = -1$ (“symplectic symmetry class”), will be reserved for future work.

ACKNOWLEDGMENTS

This work was supported by the US Department of Energy, Office of Science, Basic Energy Sciences, under Award No. DE-SC0023999. R.V. acknowledge hospitality of KITP during the DYNISQ22 follow-on program “Phases of active quantum matter” during which parts of this work were completed. K.I.T.P. was supported by NSF, Grant No. PHY-2309135. We thank Chao-Ming Jian and Andrew Potter for useful discussions.

DATA AVAILABILITY

The data that support the findings of this article are not publicly available. The data are available from the authors upon reasonable request.

APPENDIX A: (DOUBLE) COSET TYPES OF $H_N \subset S_{2N}$

(Double) Coset Types of $H_N \subset S_{2N}$ Consider the subgroup $H_N \subset S_{2N}$ generated by the transpositions $(l l')$, $1 \leq l \leq N$, and double transpositions $(l m), (l' m')$, $1 \leq l < m \leq N$. Let $\sigma \in S_{2N}$ and create an undirected graph with vertices $\{1, \dots, 2N\}$ and edges between the vertex pairs $\{l l'\}, \{\sigma(m), \sigma(m')\}$. Each vertex is then part of two edges and the number of vertices in each connected component is even. Let them be indexed as $2\lambda_1 \geq 2\lambda_2 \geq \dots \geq 2\lambda_l$ (where we have l connected components). Then $\lambda = (\lambda_1, \lambda_2, \dots, \lambda_l)$ is a partition of N (in symbols $\lambda \vdash N$), and one defines λ to be the ‘‘coset type’’ of σ . Note that this is exactly how the contraction in Eq. (8) was defined as well. Additionally, one can check that given $\sigma, \tau \in S_{2N}$, their coset types coincide iff $H_N \sigma H_N = H_N \tau H_N$ resulting in a double coset decomposition of S_{2N} with respect to the subgroup $H_N \subset S_{2N}$,

$$S_{2N} = \bigsqcup_{k \vdash N} H_k, \quad (\text{A1})$$

where $H_k := \{\sigma \in S_{2N} \mid \text{the coset type of } \sigma \text{ is } k\}$. Finally, using the definition of H_N in Sec. IV C, it is easy to show that $H_N := H_{(1)^N}$, which is the double coset of the identity permutation $e \in S_{2N}$: $H_N = H_N e H_N$.

APPENDIX B: A PROTOCOL TO MEASURE THE ANISOTROPY PARAMETER

We present the numerical protocols used to evaluate the anisotropy factor for various stat-mech models introduced in the main text. We begin with a brief review of the protocol outlined in the Appendix of Ref. [46], which we use for the local TR symmetric case. We then discuss a modified protocol that we introduce for the global TR symmetric stat-mech models (both postselected and non-postselected versions).

The free energy density $f = F/A$ is measured per unit spacetime area $A = \alpha L t$, where α measures the asymmetry between space and time with $L = \alpha t$. To measure this asymmetry, we compare correlation functions in the space and time directions at criticality. Due to conformal invariance, we can map correlation functions on our $(1+1)$ -d stat-mech models onto correlation functions on a cylinder using the conformal mapping $z' = f(z) = \frac{L}{2\pi} \ln z$. This results in the correlation function between two points $g'(z'_1, z'_2)$ on the cylinder:

$$g'(z'_1, z'_2) = \left(\frac{\pi}{L}\right)^{2\Delta} \frac{1}{|\sin[\frac{\pi}{L}(z'_1 - z'_2)]|^{2\Delta}}, \quad (\text{B1})$$

where Δ is the conformal dimension. We can extract the anisotropy factor by setting $g'_{\text{time}} := g(0, \alpha t)$ and $g'_{\text{space}} := g(0, iL/2)$. This gives

$$\frac{g'_{\text{time}}}{g'_{\text{space}}} = \left(\frac{2e^{\pi\alpha t/L}}{e^{2\pi\alpha t/L} - 1}\right)^{2\Delta}. \quad (\text{B2})$$

Setting $\frac{g'_{\text{time}}}{g'_{\text{space}}} = 1$ for some $t = t_*$ eliminates the dependence on Δ to give

$$\alpha = \ln(1 + \sqrt{2}) \frac{L}{\pi t_*}. \quad (\text{B3})$$

To implement the above numerically, we first run the dynamics until $\tau_1 = 4L$ to allow the system to equilibrate. We then measure the qubit at site x_1 and Bell entangle an ancilla qubit to it. Following that, we run the dynamics up until $\tau_2 = \tau_1 + \delta\tau$, measure at site $x_2 = x_1 + \delta x$, and similarly entangle another ancilla to this site. We then follow the mutual information between the ancillas to obtain $I_{12}(\delta x, \delta\tau)$. We use $\delta x = 0$ to obtain g'_{time} for various $\delta\tau$, and $\delta\tau = 0, \delta x = L/2$ to obtain g'_{space} .

The aforementioned protocol largely holds true but needs careful modification to apply to the case of the mirrored stat-mech model introduced in Sec. IV B 2. There are two considerations that modify our protocol. First, note that time in the stat-mech model corresponds to a vertical interval in Fig. 5, which is not the same as a time measured by the time steps of a circuit. Second, since a given spacetime point on the stat-mech model corresponds to two instances in the real-time circuit, extracting any correlation function in the stat-mech picture must involve performing an operation (such as measuring and entangling with an ancilla) at *both* a given site and its mirrored counterpart. In other words, our protocol must necessarily respect the mirror symmetry of the model while implementing the standard protocol. Here is the step-by-step procedure we use in order to achieve the above:

(1) We run the dynamics up until $\tau_1 = 20L$, after which we measure (with outcome $m_1 \in \{0, 1\}$) and entangle ancilla 1 at site x_1 .

(2) We further run the dynamics until time $\tau_2 = \tau_1 + \delta\tau$, measure the qubit at site x_2 (with outcome $m_2 \in \{0, 1\}$), and entangle a ancilla 2 to this site.

(3) We follow the dynamics for τ time steps, completing the first half of our evolution.

(4) We begin the mirrored evolution for τ time steps, using identical gates, measurement locations, and postselecting outcomes to the corresponding first half of the evolution. We skip the postselection of outcomes for the non-postselected global TR model as discussed in Sec. IV B 2.

(5) We store the qubit at site x_2 and replace it with a qubit at this site in state $|m_2\rangle$. This is the mirror operation of measuring at site x_2 and bell-entangling it with an ancilla. One can think of the stored qubit as a mirrored ancilla and the replaced qubit as mirror of the measured qubit in the forward evolution.

(6) We evolve the system for time $\delta\tau$ and perform the same procedure of storing the qubit at site x_1 and replacing it with a qubit in the state $|m_1\rangle$.

(7) We follow the mirrored dynamics for the rest of the time ($20L$) while keeping track of the mutual information $I_{12}(\delta x, \delta\tau)$ between the systems 1 \equiv {qubit at site x_1 + ancilla 1} and 2 \equiv {qubit at site x_2 + ancilla 2}.

It is important to note that τ introduced above is the time in our stat-mech model [as shown in Figs. 9(b) and 9(c)], and it is with respect to this time that we must record I_{12} . In particular,

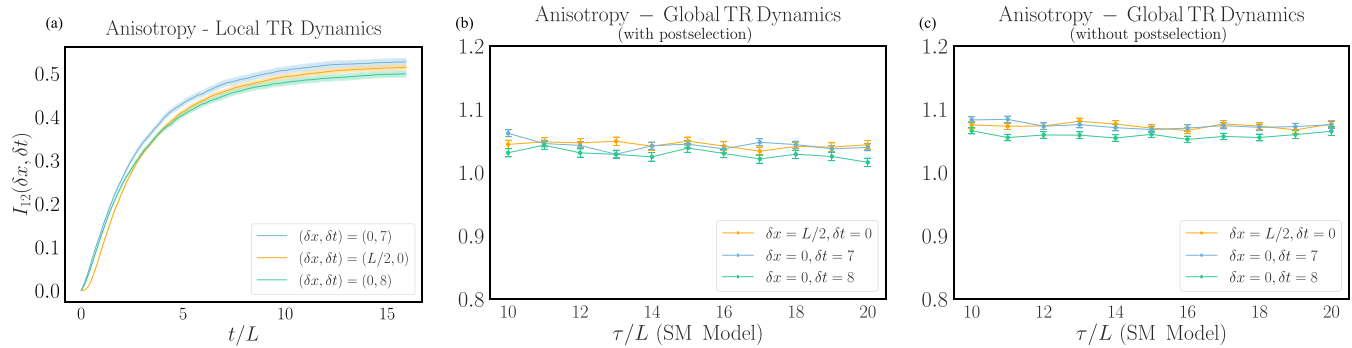


FIG. 9. Space and time correlation functions for calculating anisotropy for Haar TR models: These are plotted at p_c of various TR symmetric models discussed in the main text for size $L = 16$ (a) Local TR dynamics. Each point above is sampled from over 3000 circuits. (b) Global TR dynamics without postselection. Each point is sampled from over 20000 circuits. (c) Global TR dynamics with postselection. Each point above is sampled from over 20000 circuits.

this implies that in order to get I_{12} vs τ , one must repeat the above procedure for different values of τ .

APPENDIX C: p_c AND ANISOTROPY FACTORS FOR HAAR RANDOM TR SYMMETRIC MODELS

1. p_c for Haar TR models

We obtain the critical point for the Haar random TR models using TMI $I_{3,n=1}$ as a probe [16,28]. TMI is defined as

$$I_{3,n} = S_n(A) + S_n(B) + S_n(C) - S_n(A \cup B) - S_n(B \cup C) - S_n(C \cup A) + S_n(A \cup B \cup C), \quad (C1)$$

where $S_n(A)$ is the subsystem Rényi entropy defined in Eq. (1), and regions A, B, and C are consecutive sections of the chain of length $L/4$, where L is the length of the full chain. The resulting plots are shown in Fig. 8.

2. Anisotropy for Haar TR models

The result of the above procedures is displayed in Fig. 9. We obtain records of $g_{\text{space}}(\delta x = N/2)$ and $g_{\text{time}}(\delta \tau)$ at their respective p_c so that $g_{\text{time}}(\delta \tau) \leq g_{\text{space}} \leq g_{\text{time}}(\delta \tau + 1)$. We then linearly interpolate to find the matching time t_* and use Eq. (B3) to obtain the anisotropy factor [46]. For local TR dynamics, we estimate the matching time $t_* \approx 7.51$, which results in $\alpha_{\text{local}} \approx 0.59(5)$. For the global TR case (with postselection), we observe that the correlation functions settle at $\tau \approx 10L$, where τ is time in the statistical mechanics model. We estimate α_{global} as the average of the anisotropy factors obtained from each of the data points in Fig. 9(b), resulting in $\alpha_{\text{global}} \approx 0.61(8)$. In the same manner we obtain, resulting in $\alpha_{\text{global}^*} \approx 0.64(6)$ for the non-postselected version of the global TR model.

- [1] J. M. Deutsch, Quantum statistical mechanics in a closed system, *Phys. Rev. A* **43**, 2046 (1991).
- [2] M. Srednicki, Chaos and quantum thermalization, *Phys. Rev. E* **50**, 888 (1994).
- [3] M. Rigol, V. Dunjko, and M. Olshanii, Thermalization and its mechanism for generic isolated quantum systems, *Nature (London)* **452**, 854 (2008).
- [4] D. A. Abanin, E. Altman, I. Bloch, and M. Serbyn, *Colloquium: Many-body localization, thermalization, and entanglement*, *Rev. Mod. Phys.* **91**, 021001 (2019).
- [5] I. M. Georgescu, S. Ashhab, and F. Nori, Quantum simulation, *Rev. Mod. Phys.* **86**, 153 (2014).
- [6] J. Preskill, Quantum computing in the NISQ era and beyond, *Quantum* **2**, 79 (2018).
- [7] M. Kardar, G. Parisi, and Y.-C. Zhang, Dynamic scaling of growing interfaces, *Phys. Rev. Lett.* **56**, 889 (1986).
- [8] A. Nahum, J. Ruhman, S. Vijay, and J. Haah, Quantum entanglement growth under random unitary dynamics, *Phys. Rev. X* **7**, 031016 (2017).
- [9] T. Zhou and A. Nahum, Emergent statistical mechanics of entanglement in random unitary circuits, *Phys. Rev. B* **99**, 174205 (2019).
- [10] S. Ryu and T. Takayanagi, Holographic derivation of entanglement entropy from antide Sitter Space/Conformal Field Theory Correspondence, *Phys. Rev. Lett.* **96**, 181602 (2006).
- [11] S. Ryu and T. Takayanagi, Aspects of holographic entanglement entropy, *J. High Energy Phys.* **08** (2006) 045.
- [12] C. W. von Keyserlingk, T. Rakovszky, F. Pollmann, and S. L. Sondhi, Operator hydrodynamics, OTOCs, and entanglement growth in systems without conservation laws, *Phys. Rev. X* **8**, 021013 (2018).
- [13] A. Nahum, S. Vijay, and J. Haah, Operator spreading in random unitary circuits, *Phys. Rev. X* **8**, 021014 (2018).
- [14] B. Skinner, J. Ruhman, and A. Nahum, Measurement-induced phase transitions in the dynamics of entanglement, *Phys. Rev. X* **9**, 031009 (2019).
- [15] Y. Li, X. Chen, and M. P. A. Fisher, Quantum Zeno effect and the many-body entanglement transition, *Phys. Rev. B* **98**, 205136 (2018).
- [16] M. J. Gullans and D. A. Huse, Dynamical purification phase transition induced by quantum measurements, *Phys. Rev. X* **10**, 041020 (2020).
- [17] S. Choi, Y. Bao, X.-L. Qi, and E. Altman, Quantum error correction in scrambling dynamics and measurement-induced phase transition, *Phys. Rev. Lett.* **125**, 030505 (2020).
- [18] F. Barratt, U. Agrawal, A. C. Potter, S. Gopalakrishnan, and R. Vasseur, Transitions in the learnability of global charges from local measurements, *Phys. Rev. Lett.* **129**, 200602 (2022).

- [19] M. Ippoliti and V. Khemani, Learnability transitions in monitored quantum dynamics via eavesdropper's classical shadows, *PRX Quantum* **5**, 020304 (2024).
- [20] Y. Li and M. P. A. Fisher, Statistical mechanics of quantum error correcting codes, *Phys. Rev. B* **103**, 104306 (2021).
- [21] R. Fan, S. Vijay, A. Vishwanath, and Y.-Z. You, Self-organized error correction in random unitary circuits with measurement, *Phys. Rev. B* **103**, 174309 (2021).
- [22] Y. Li, X. Chen, and M. P. A. Fisher, Measurement-driven entanglement transition in hybrid quantum circuits, *Phys. Rev. B* **100**, 134306 (2019).
- [23] A. Chan, R. M. Nandkishore, M. Pretko, and G. Smith, Unitary-projective entanglement dynamics, *Phys. Rev. B* **99**, 224307 (2019).
- [24] Y. Li, X. Chen, A. W. W. Ludwig, and M. P. A. Fisher, Conformal invariance and quantum nonlocality in critical hybrid circuits, *Phys. Rev. B* **104**, 104305 (2021).
- [25] X. Cao, A. Tilloy, and A. D. Luca, Entanglement in a fermion chain under continuous monitoring, *SciPost Phys.* **7**, 024 (2019).
- [26] M. Szyniszewski, A. Romito, and H. Schomerus, Entanglement transition from variable-strength weak measurements, *Phys. Rev. B* **100**, 064204 (2019).
- [27] M. J. Gullans and D. A. Huse, Scalable probes of measurement-induced criticality, *Phys. Rev. Lett.* **125**, 070606 (2020).
- [28] A. Zabalo, M. J. Gullans, J. H. Wilson, S. Gopalakrishnan, D. A. Huse, and J. H. Pixley, Critical properties of the measurement-induced transition in random quantum circuits, *Phys. Rev. B* **101**, 060301 (2020).
- [29] A. Nahum and B. Skinner, Entanglement and dynamics of diffusion-annihilation processes with Majorana defects, *Phys. Rev. Res.* **2**, 023288 (2020).
- [30] M. Ippoliti, M. J. Gullans, S. Gopalakrishnan, D. A. Huse, and V. Khemani, Entanglement phase transitions in measurement-only dynamics, *Phys. Rev. X* **11**, 011030 (2021).
- [31] A. Lavasani, Y. Alavirad, and M. Barkeshli, Measurement-induced topological entanglement transitions in symmetric random quantum circuits, *Nat. Phys.* **17**, 342 (2021).
- [32] S. Sang and T. H. Hsieh, Measurement-protected quantum phases, *Phys. Rev. Res.* **3**, 023200 (2021).
- [33] Q. Tang and W. Zhu, Measurement-induced phase transition: A case study in the nonintegrable model by density-matrix renormalization group calculations, *Phys. Rev. Res.* **2**, 013022 (2020).
- [34] X. Turkeshi, R. Fazio, and M. Dalmonte, Measurement-induced criticality in $(2+1)$ -dimensional hybrid quantum circuits, *Phys. Rev. B* **102**, 014315 (2020).
- [35] Y. Fuji and Y. Ashida, Measurement-induced quantum criticality under continuous monitoring, *Phys. Rev. B* **102**, 054302 (2020).
- [36] O. Lunt, M. Szyniszewski, and A. Pal, Measurement-induced criticality and entanglement clusters: A study of one-dimensional and two-dimensional Clifford circuits, *Phys. Rev. B* **104**, 155111 (2021).
- [37] X. Turkeshi, A. Biella, R. Fazio, M. Dalmonte, and M. Schiró, Measurement-induced entanglement transitions in the quantum Ising chain: From infinite to zero clicks, *Phys. Rev. B* **103**, 224210 (2021).
- [38] M. Ippoliti and V. Khemani, Postselection-free entanglement dynamics via spacetime duality, *Phys. Rev. Lett.* **126**, 060501 (2021).
- [39] T.-C. Lu and T. Grover, Spacetime duality between localization transitions and measurement-induced transitions, *PRX Quantum* **2**, 040319 (2021).
- [40] C.-M. Jian, B. Bauer, A. Keselman, and A. W. W. Ludwig, Criticality and entanglement in nonunitary quantum circuits and tensor networks of noninteracting fermions, *Phys. Rev. B* **106**, 134206 (2022).
- [41] S. Gopalakrishnan and M. J. Gullans, Entanglement and purification transitions in non-Hermitian quantum mechanics, *Phys. Rev. Lett.* **126**, 170503 (2021).
- [42] X. Turkeshi, Measurement-induced criticality as a data-structure transition, *Phys. Rev. B* **106**, 144313 (2022).
- [43] Y. Bao, S. Choi, and E. Altman, Symmetry enriched phases of quantum circuits, *Ann. Phys.* **435**, 168618 (2021).
- [44] M. Block, Y. Bao, S. Choi, E. Altman, and N. Y. Yao, Measurement-induced transition in long-range interacting quantum circuits, *Phys. Rev. Lett.* **128**, 010604 (2022).
- [45] G. S. Bentsen, S. Sahu, and B. Swingle, Measurement-induced purification in large- n hybrid Brownian circuits, *Phys. Rev. B* **104**, 094304 (2021).
- [46] A. Zabalo, M. J. Gullans, J. H. Wilson, R. Vasseur, A. W. W. Ludwig, S. Gopalakrishnan, D. A. Huse, and J. H. Pixley, Operator scaling dimensions and multifractality at measurement-induced transitions, *Phys. Rev. Lett.* **128**, 050602 (2022).
- [47] U. Agrawal, A. Zabalo, K. Chen, J. H. Wilson, A. C. Potter, J. H. Pixley, S. Gopalakrishnan, and R. Vasseur, Entanglement and charge-sharpening transitions in $U(1)$ symmetric monitored quantum circuits, *Phys. Rev. X* **12**, 041002 (2022).
- [48] Y. Li and M. P. A. Fisher, Decodable hybrid dynamics of open quantum systems with \mathbb{Z}_2 symmetry, *Phys. Rev. B* **108**, 214302 (2023).
- [49] O. Alberton, M. Buchhold, and S. Diehl, Entanglement transition in a monitored free-fermion chain: From extended criticality to area law, *Phys. Rev. Lett.* **126**, 170602 (2021).
- [50] S.-K. Jian, C. Liu, X. Chen, B. Swingle, and P. Zhang, Quantum error as an emergent magnetic field, [arXiv:2106.09635](https://arxiv.org/abs/2106.09635).
- [51] E. V. H. Doggen, Y. Gefen, I. V. Gornyi, A. D. Mirlin, and D. G. Polyakov, Generalized quantum measurements with matrix product states: Entanglement phase transition and clusterization, *Phys. Rev. Res.* **4**, 023146 (2022).
- [52] P. Sierant and X. Turkeshi, Universal behavior beyond multifractality of wave functions at measurement-induced phase transitions, *Phys. Rev. Lett.* **128**, 130605 (2022).
- [53] M. Buchhold, Y. Minoguchi, A. Altland, and S. Diehl, Effective theory for the measurement-induced phase transition of Dirac fermions, *Phys. Rev. X* **11**, 041004 (2021).
- [54] P. Sierant, G. Chiriaco, F. M. Surace, S. Sharma, X. Turkeshi, M. Dalmonte, R. Fazio, and G. Pagano, Dissipative Floquet dynamics: From steady state to measurement induced criticality in trapped-ion chains, *Quantum* **6**, 638 (2022).
- [55] S. Sharma, X. Turkeshi, R. Fazio, and M. Dalmonte, Measurement-induced criticality in extended and long-range unitary circuits, *SciPost Phys. Core* **5**, 023 (2022).
- [56] Y. Li, Y. Zou, P. Glorioso, E. Altman, and M. P. A. Fisher, Cross entropy benchmark for measurement-induced phase transitions, *Phys. Rev. Lett.* **130**, 220404 (2023).

- [57] A.-R. Negari, S. Sahu, and T. H. Hsieh, Measurement-induced phase transitions in the toric code, *Phys. Rev. B* **109**, 125148 (2024).
- [58] G. Cecile, H. Lóio, and J. De Nardis, Measurement-induced phase transitions by matrix product states scaling, *Phys. Rev. Res.* **6**, 033220 (2024).
- [59] X. Feng, B. Skinner, and A. Nahum, Measurement-induced phase transitions on dynamical quantum trees, *PRX Quantum* **4**, 030333 (2023).
- [60] E. Heinrich and X. Chen, Measurement-induced phase transitions in quantum raise-and-peel models, *Phys. Rev. B* **110**, 064309 (2024).
- [61] K. Aziz, A. Chakraborty, and J. H. Pixley, Critical properties of weak measurement induced phase transitions in random quantum circuits, *Phys. Rev. B* **110**, 064301 (2024).
- [62] T. Jin and D. G. Martin, Measurement-induced phase transition in a single-body tight-binding model, *Phys. Rev. B* **110**, L060202 (2024).
- [63] A. Paviglianiti and A. Silva, Multipartite entanglement in the measurement-induced phase transition of the quantum Ising chain, *Phys. Rev. B* **108**, 184302 (2023).
- [64] A. Zabalo, J. H. Wilson, M. J. Gullans, R. Vasseur, S. Gopalakrishnan, D. A. Huse, and J. H. Pixley, Infinite-randomness criticality in monitored quantum dynamics with static disorder, *Phys. Rev. B* **107**, L220204 (2023).
- [65] G. Shkolnik, A. Zabalo, R. Vasseur, D. A. Huse, J. H. Pixley, and S. Gazit, Measurement induced criticality in quasiperiodic modulated random hybrid circuits, *Phys. Rev. B* **108**, 184204 (2023).
- [66] A. Kumar, K. Aziz, A. Chakraborty, A. W. W. Ludwig, S. Gopalakrishnan, J. H. Pixley, and R. Vasseur, Boundary transfer matrix spectrum of measurement-induced transitions, *Phys. Rev. B* **109**, 014303 (2024).
- [67] S. Liu, M.-R. Li, S.-X. Zhang, S.-K. Jian, and H. Yao, Universal Kardar-Parisi-Zhang scaling in noisy hybrid quantum circuits, *Phys. Rev. B* **107**, L201113 (2023).
- [68] Y. L. Gal, X. Turkeshi, and M. Schirò, Entanglement dynamics in monitored systems and the role of quantum jumps, *PRX Quantum* **5**, 030329 (2024).
- [69] H. Pan, S. Ganeshan, T. Iadecola, J. H. Wilson, and J. H. Pixley, Local and nonlocal stochastic control of quantum chaos: Measurement- and control-induced criticality, *Phys. Rev. B* **110**, 054308 (2024).
- [70] L. Lumia, E. Tirrito, R. Fazio, and M. Collura, Measurement-induced transitions beyond gaussianity: A single particle description, *Phys. Rev. Res.* **6**, 023176 (2024).
- [71] P. Sierant and X. Turkeshi, Controlling entanglement at absorbing state phase transitions in random circuits, *Phys. Rev. Lett.* **130**, 120402 (2023).
- [72] S. Liu, M.-R. Li, S.-X. Zhang, and S.-K. Jian, Entanglement structure and information protection in noisy hybrid quantum circuits, *Phys. Rev. Lett.* **132**, 240402 (2024).
- [73] E. Granet, C. Zhang, and H. Dreyer, Volume-law to area-law entanglement transition in a nonunitary periodic Gaussian circuit, *Phys. Rev. Lett.* **130**, 230401 (2023).
- [74] K. Yamamoto and R. Hamazaki, Localization properties in disordered quantum many-body dynamics under continuous measurement, *Phys. Rev. B* **107**, L220201 (2023).
- [75] A. Chakraborty, K. Chen, A. Zabalo, J. H. Wilson, and J. H. Pixley, Charge and entanglement criticality in a $U(1)$ -symmetric hybrid circuit of qubits, *Phys. Rev. B* **110**, 045135 (2024).
- [76] V. Ravindranath, Y. Han, Z.-C. Yang, and X. Chen, Entanglement steering in adaptive circuits with feedback, *Phys. Rev. B* **108**, L041103 (2023).
- [77] X. Feng, S. Liu, S. Chen, and W. Guo, Absence of logarithmic and algebraic scaling entanglement phases due to the skin effect, *Phys. Rev. B* **107**, 094309 (2023).
- [78] S. Liu, M.-R. Li, S.-X. Zhang, S.-K. Jian, and H. Yao, Noise-induced phase transitions in hybrid quantum circuits, *Phys. Rev. B* **110**, 064323 (2024).
- [79] H. Oshima and Y. Fuji, Charge fluctuation and charge-resolved entanglement in a monitored quantum circuit with $U(1)$ symmetry, *Phys. Rev. B* **107**, 014308 (2023).
- [80] L. Piroli, Y. Li, R. Vasseur, and A. Nahum, Triviality of quantum trajectories close to a directed percolation transition, *Phys. Rev. B* **107**, 224303 (2023).
- [81] T. Iadecola, S. Ganeshan, J. H. Pixley, and J. H. Wilson, Measurement and feedback driven entanglement transition in the probabilistic control of chaos, *Phys. Rev. Lett.* **131**, 060403 (2023).
- [82] Z. Weinstein, S. P. Kelly, J. Marino, and E. Altman, Scrambling transition in a radiative random unitary circuit, *Phys. Rev. Lett.* **131**, 220404 (2023).
- [83] Y. Li and M. Claassen, Statistical mechanics of monitored dissipative random circuits, *Phys. Rev. B* **108**, 104310 (2023).
- [84] M. Szyniszewski, O. Lunt, and A. Pal, Disordered monitored free fermions, *Phys. Rev. B* **108**, 165126 (2023).
- [85] A. Nahum and K. J. Wiese, Renormalization group for measurement and entanglement phase transitions, *Phys. Rev. B* **108**, 104203 (2023).
- [86] J. Merritt and L. Fidkowski, Entanglement transitions with free fermions, *Phys. Rev. B* **107**, 064303 (2023).
- [87] Y. Li, S. Vijay, and M. P. Fisher, Entanglement domain walls in monitored quantum circuits and the directed polymer in a random environment, *PRX Quantum* **4**, 010331 (2023).
- [88] H. Lóio, A. De Luca, J. De Nardis, and X. Turkeshi, Purification timescales in monitored fermions, *Phys. Rev. B* **108**, L020306 (2023).
- [89] C.-M. Jian, H. Shapourian, B. Bauer, and A. W. W. Ludwig, Measurement-induced entanglement transitions in quantum circuits of non-interacting fermions: Born-rule versus forced measurements, *arXiv:2302.09094*.
- [90] M. Fava, L. Piroli, T. Swann, D. Bernard, and A. Nahum, Non-linear sigma models for monitored dynamics of free fermions, *Phys. Rev. X* **13**, 041045 (2023).
- [91] I. Poboiko, P. Pöpperl, I. V. Gornyi, and A. D. Mirlin, Theory of free fermions under random projective measurements, *Phys. Rev. X* **13**, 041046 (2023).
- [92] S. Sang, Z. Li, T. H. Hsieh, and B. Yoshida, Ultrafast entanglement dynamics in monitored quantum circuits, *PRX Quantum* **4**, 040332 (2023).
- [93] A. C. Potter and R. Vasseur, Entanglement dynamics in hybrid quantum circuits, in *Entanglement in Spin Chains* (Springer International Publishing, Berlin, 2022), pp. 211–249.
- [94] M. P. Fisher, V. Khemani, A. Nahum, and S. Vijay, Random quantum circuits, *Annu. Rev. Condens. Matter Phys.* **14**, 335 (2023).
- [95] C. Noel, P. Niroula, D. Zhu, A. Risinger, L. Egan, D. Biswas, M. Cetina, A. V. Gorshkov, M. J. Gullans, D.A. Huse, and

- C. Monroe, Measurement-induced quantum phases realized in a trapped-ion quantum computer, *Nat. Phys.* **18**, 760 (2022).
- [96] J. M. Koh, S.-N. Sun, M. Motta, and A. J. Minnich, Measurement-induced entanglement phase transition on a superconducting quantum processor with mid-circuit readout, *Nat. Phys.* **19**, 1314 (2023).
- [97] Google Quantum AI and Collaborators, Measurement-induced entanglement and teleportation on a noisy quantum processor, *Nature (London)* **622**, 481 (2023).
- [98] U. Agrawal, J. Lopez-Piqueres, R. Vasseur, S. Gopalakrishnan, and A. C. Potter, Observing quantum measurement collapse as a learnability phase transition, *Phys. Rev. X* **14**, 041012 (2024).
- [99] H. Kamakari, J. Sun, Y. Li, J. J. Thio, T. P. Gujarati, M. P. A. Fisher, M. Motta, and A. J. Minnich, Experimental demonstration of scalable cross-entropy benchmarking to detect measurement-induced phase transitions on a superconducting quantum processor, *Phys. Rev. Lett.* **134**, 120401 (2025).
- [100] P. Hayden, S. Nezami, X.-L. Qi, N. Thomas, M. Walter, and Z. Yang, Holographic duality from random tensor networks, *J. High Energy Phys.* **11** (2016) 009.
- [101] R. Vasseur, A. C. Potter, Y.-Z. You, and A. W. W. Ludwig, Entanglement transitions from holographic random tensor networks, *Phys. Rev. B* **100**, 134203 (2019).
- [102] Y. Bao, S. Choi, and E. Altman, Theory of the phase transition in random unitary circuits with measurements, *Phys. Rev. B* **101**, 104301 (2020).
- [103] C.-M. Jian, Y.-Z. You, R. Vasseur, and A. W. W. Ludwig, Measurement-induced criticality in random quantum circuits, *Phys. Rev. B* **101**, 104302 (2020).
- [104] Y. Li, R. Vasseur, M. P. A. Fisher, and A. W. W. Ludwig, Statistical mechanics model for Clifford random tensor networks and monitored quantum circuits, *Phys. Rev. B* **109**, 174307 (2024).
- [105] A. J. Friedman, A. Chan, A. De Luca, and J. T. Chalker, Spectral statistics and many-body quantum chaos with conserved charge, *Phys. Rev. Lett.* **123**, 210603 (2019).
- [106] T. Rakovszky, F. Pollmann, and C. W. von Keyserlingk, Diffusive hydrodynamics of out-of-time-ordered correlators with charge conservation, *Phys. Rev. X* **8**, 031058 (2018).
- [107] V. Khemani, A. Vishwanath, and D. A. Huse, Operator spreading and the emergence of dissipative hydrodynamics under unitary evolution with conservation laws, *Phys. Rev. X* **8**, 031057 (2018).
- [108] S. Majidy, U. Agrawal, S. Gopalakrishnan, A. C. Potter, R. Vasseur, and N. Y. Halpern, Critical phase and spin sharpening in SU(2)-symmetric monitored quantum circuits, *Phys. Rev. B* **108**, 054307 (2023).
- [109] E. McCulloch, J. De Nardis, S. Gopalakrishnan, and R. Vasseur, Full counting statistics of charge in chaotic many-body quantum systems, *Phys. Rev. Lett.* **131**, 210402 (2023).
- [110] H. Guo, M. S. Foster, C.-M. Jian, and A. W. W. Ludwig, Field theory of monitored, interacting fermion dynamics with charge conservation, *Phys. Rev. B* **112**, 064304, (2025).
- [111] I. Poboiko, P. Pöpperl, I. V. Gornyi, and A. D. Mirlin, Measurement-induced transitions for interacting fermions, *Phys. Rev. B* **111**, 024204 (2025).
- [112] F. J. Dyson, Statistical theory of the energy levels of complex systems. I, *J. Math. Phys.* **3**, 140 (1962).
- [113] M. R. Zirnbauer, Riemannian symmetric superspaces and their origin in random-matrix theory, *J. Math. Phys.* **37**, 4986 (1996).
- [114] A. Altland and M. R. Zirnbauer, Nonstandard symmetry classes in mesoscopic normal-superconducting hybrid structures, *Phys. Rev. B* **55**, 1142 (1997).
- [115] P. Heinzner, A. Huckleberry, and M. Zirnbauer, Symmetry classes of disordered fermions, *Commun. Math. Phys.* **257**, 725 (2005).
- [116] A. W. W. Ludwig, Topological phases: Classification of topological insulators and superconductors of non-interacting fermions, and beyond, *Phys. Scr.* **2016**, 014001 (2015).
- [117] A.P. Schnyder, S. Ryu, A. Furusaki, and A. W. W. Ludwig, Classification of topological insulators and superconductors in three spatial dimensions, *Phys. Rev. B* **78**, 195125 (2008).
- [118] S. Ryu, A. P. Schnyder, A. Furusaki, and A. W. W. Ludwig, Topological insulators and superconductors: Ten-fold way and dimensional hierarchy, *New J. Phys.* **12**, 065010 (2010).
- [119] L. Fidkowski and A. Kitaev, Topological phases of fermions in one dimension, *Phys. Rev. B* **83**, 075103 (2011).
- [120] C. Wang and T. Senthil, Interacting fermionic topological insulators/superconductors in three dimensions, *Phys. Rev. B* **89**, 195124 (2014).
- [121] H. Pan, H. Shapourian, and C.-M. Jian, Topological modes in monitored quantum dynamics, *Phys. Rev. B* **112**, 144301 (2025).
- [122] S. Matsumoto, General moments of matrix elements from circular orthogonal ensembles, *Random Matrices Theory Appl.* **01**, 1250005 (2012).
- [123] N. Hunter-Jones, Operator growth in random quantum circuits with symmetry, [arXiv:1812.08219](https://arxiv.org/abs/1812.08219).
- [124] T. Kalsi, A. Romito, and H. Schomerus, Three-fold way of entanglement dynamics in monitored quantum circuits, *J. Phys. A: Math. Theor.* **55**, 264009 (2022).
- [125] A. Khindanov, I. L. Aleiner, L. Faoro, and L. B. Ioffe, Observable measurement-induced transitions, *Ann. Phys.* **479**, 170047 (2025).
- [126] X. Turkeshi and P. Sierant, Error-resilience phase transitions in encoding-decoding quantum circuits, *Phys. Rev. Lett.* **132**, 140401 (2024).
- [127] P. Niroula, C. D. White, Q. Wang, S. Johri, D. Zhu, C. Monroe, C. Noel, and M. J. Gullans, Phase transition in magic with random quantum circuits, *Nat. Phys.* **20**, 1786 (2024).
- [128] J. J. Sakurai and J. Napolitano, *Modern Quantum Mechanics*, 3rd ed. (Cambridge University Press, Cambridge, 2020).
- [129] M. L. Mehta, *Random Matrices* (Academic Press, New York, NY, 1967).
- [130] E. Cartan, Sur une classe remarquable d'espaces de Riemann, *Bul. Soc. Math. France* **2**, 214 (1926).
- [131] S. Helgason, *Differential Geometry, Lie Groups, and Symmetric Spaces*, Graduate Studies in Mathematics Vol. 34 (American Mathematical Society, Providence, RI, 1978).
- [132] B. Collins and P. Śniady, Integration with respect to the Haar measure on unitary, orthogonal and symplectic group, *Commun. Math. Phys.* **264**, 773 (2006).
- [133] B. Collins and S. Matsumoto, On some properties of orthogonal Weingarten functions, *J. Math. Phys.* **50**, 113516 (2009).
- [134] R. Fan, Y. Bao, E. Altman, and A. Vishwanath, Diagnostics of mixed-state topological order and breakdown of quantum memory, *PRX Quantum* **5**, 020343 (2024).

- [135] J. C. Napp, R. L. La Placa, A. M. Dalzell, F. G. S. L. Brandão, and A. W. Harrow, Efficient classical simulation of random shallow 2D quantum circuits, *Phys. Rev. X* **12**, 021021 (2022).
- [136] Mathematically, this can be seen as follows. $Wg^{O(D+1)}(\tau)$ comprises of a linear combination of the unitary Weingarten function $Wg_D(\sigma^{-1}\tau)$ and the graphical contraction being summed over in Eq. (8). The unitary Weingarten functions are symmetric under $S_{2N} \times S_{2N}$ since they are class functions. The contractions, on the other hand, define the *coset type* of the double cosets of the group $H_N \times H_N$ in S_{2N} [122] (see Appendix A). Since coset types of two permutations $\sigma, \tau \in S_{2N}$ coincide iff they are connected by the conjugate action of $H_N \times H_N$ by definition, such that $\sigma = h_1\tau h_2^{-1}$, $h_1, h_2 \in H_N$, the graphical contractions are symmetric under $H_N \times H_N$. Consequently, $Wg^{O(D+1)}(\tau)$ is constant over the different double cosets of $H_N \subset S_{2N}$.
- [137] D. Gross, S. Nezami, and M. Walter, Schur–Weyl duality for the Clifford group with applications: Property testing, a Robust Hudson theorem, and de Finetti representations, *Commun. Math. Phys.* **385**, 1325 (2021).
- [138] H. Dehghani, A. Lavasani, M. Hafezi, and M. J. Gullans, Neural-network decoders for measurement induced phase transitions, *Nat. Commun.* **14**, 2918 (2023).
- [139] S. J. Garratt, Z. Weinstein, and E. Altman, Measurements conspire nonlocally to restructure critical quantum states, *Phys. Rev. X* **13**, 021026 (2023).
- [140] J. Y. Lee, W. Ji, Z. Bi, and M. P. A. Fisher, Decoding measurement-prepared quantum phases and transitions: From Ising model to gauge theory, and beyond, [arXiv:2208.11699](https://arxiv.org/abs/2208.11699).
- [141] S. J. Garratt and E. Altman, Probing postmeasurement entanglement without postselection, *PRX Quantum* **5**, 030311 (2024).
- [142] R. Barends, J. Kelly, A. Megrant, A. Veitia, D. Sank, E. Jeffrey, T. C. White, J. Mutus, A. G. Fowler, B. Campbell *et al.*, Superconducting quantum circuits at the surface code threshold for fault tolerance, *Nature (London)* **508**, 500 (2014).
- [143] There is a minor but subtle change to this statement for the global postselected scenario. Using Eq. (18), we see that the replicated annealed averaged partition function $\bar{Z}^k = \sum_{\mathbf{m}} p_{\mathbf{m}}^k q_{\mathbf{m}}$, where we use the born probability $q_{\mathbf{m}} \neq p_{\mathbf{m}}$ of only the first half of the trajectory to weigh each term in the partition function $Z_{\mathbf{m}}^k$. It follows from this that $F = -\sum_{\mathbf{m}} q_{\mathbf{m}} \ln p_{\mathbf{m}}$ for the global postselected case, which is *not* the (Shannon) entropy of the measurement record as is the case for the local TR-symmetric and Haar models.